

Engineering chiral topological superconductivity in twisted Ising superconductorsXiaodong Hu  and Ying Ran*Department of Physics, Boston College, Chestnut Hill, Massachusetts 02467, USA* (Received 2 June 2022; revised 26 August 2022; accepted 13 September 2022; published 21 September 2022)

van der Waals materials such as NbSe₂ or TaS₂ have demonstrated Ising superconductivity down to atomically thin layers. Due to the spin-orbit coupling, these superconductors have an in-plane upper critical magnetic field far beyond the Pauli limit. We theoretically demonstrate that twisted bilayer Ising superconductors separated by a *ferromagnetic* buffer layer can naturally host chiral topological superconductivity with Chern numbers, which can be realized in heterostructures such as NbSe₂/CrCl₃/NbSe₂. Under appropriate experimental conditions the topological superconducting gap can reach >0.1 meV, leading to readily observable signatures such as quantized thermal Hall transport at low temperatures.

DOI: [10.1103/PhysRevB.106.125136](https://doi.org/10.1103/PhysRevB.106.125136)**I. INTRODUCTION**

Transition metal dichalcogenides (TMDs) are van der Waals (vdW) materials and can be prepared as two-dimensional (2D) atomic crystals. They have attracted considerable interest and have demonstrated rich electronic phenomena ranging from charge-density-wave order, superconductivity, and exciton formation to the optical control of the valley degrees of freedom [1–5]. Strikingly, when prepared in few-layer forms, the so-called Ising superconductors gated *2H*-MoS₂, *2H*-NbSe₂, *2H*-TaS₂, *2H*-NbS₂, and *2H*-TaSe₂ have an anomalously large in-plane upper critical field, several times beyond the Pauli limit [6–11]. The physical reason for this behavior can be attributed to strong Ising spin-orbit coupling (SOC) in these materials, which pins the electrons' spin along the *z* direction and is much less susceptible to an in-plane magnetic field.

Due to their 2D nature, TMDs allow the fabrication of various vdW heterostructures with flexible tunability and interplay between electronic structures, superconductivity, and magnetism. For instance, the ferromagnetic proximity effect in monolayer TMDs has been well characterized in heterostructures such as WSe₂/CrI₃ [12–14] via optical probes. More recently, ferromagnetic Josephson junction NbSe₂/Cr₂Ge₂Te₆/NbSe₂ heterostructures have been fabricated and investigated, and an unconventional Josephson phase is reported [15,16].

On the other hand, a new paradigm in the engineering of quantum phases of matter has been recently developed based on moiré patterns [17–19] introduced by stacking 2D crystals with twisting angles. Motivated by the discovery of correlated insulators and superconductivity in twisted bilayer graphene, the idea of moiré engineering has been extended to other materials including TMDs [20–23].

Interestingly, recent theories pointed out that twisted bilayer cuprate (Bi2212) may realize chiral topological superconductivity with nonzero Chern numbers [24–26]—a novel state of matter that has yet to be experimentally confirmed,

which has triggered further experimental and theoretical investigations [27,28]. The crucial mechanism of realizing nontrivial topology here is based on the nodal superconductivity, due to sign changes of the pairing order parameter around the Fermi surface. Intuitively, nodal superconductors are naturally located on the boundary between trivial and nontrivial band topology, and engineering topological phases via perturbations becomes possible.

In order to fabricate moiré structures, vdW 2D crystals are highly desirable. Practically, however, Bi2212 may be the only known nodal superconductor among vdW 2D crystals. This puts forward a serious constraint on the moiré engineering of topological superconductivity. For example, the TMD superconductors are known to be nodeless and *s* – wave superconductors, despite theoretical discussions of the role played by magnetic fluctuations in the pairing mechanism [29]. It would be unfortunate if they cannot be included in the moiré engineering of topological superconductivity, especially considering their fabrication flexibility and tunability.

Motivated by these experimental and theoretical efforts, we ask the following question: Is it possible to moiré-engineer topological superconductivity in TMD superconductors? The answer is in the affirmative. We find that twisted Ising superconductors such as *2H*-NbSe₂ and *2H*-TaS₂ in the presence of a proximity-induced in-plane Zeeman field (beyond the Pauli limit) and out-of-plane supercurrent can host chiral topological superconductivity with Chern number 12 or 6. The topological phases are found to be robust and occupy physically realizable parameter regimes. Under proper experimental conditions the topological pairing gap is >0.1 meV.

Not surprisingly, the mechanism underlying our proposal still involves pairing-gap-closing nodes, required by a trivial-to-topological phase transition. Here, the pairing nodes are induced by the in-plane Zeeman field (beyond the Pauli limit) for Ising superconductors with Fermi pockets around the Γ point in the momentum space.

In our proposed heterostructures this in-plane Zeeman field is achieved via the magnetic proximity effect by *introducing a*

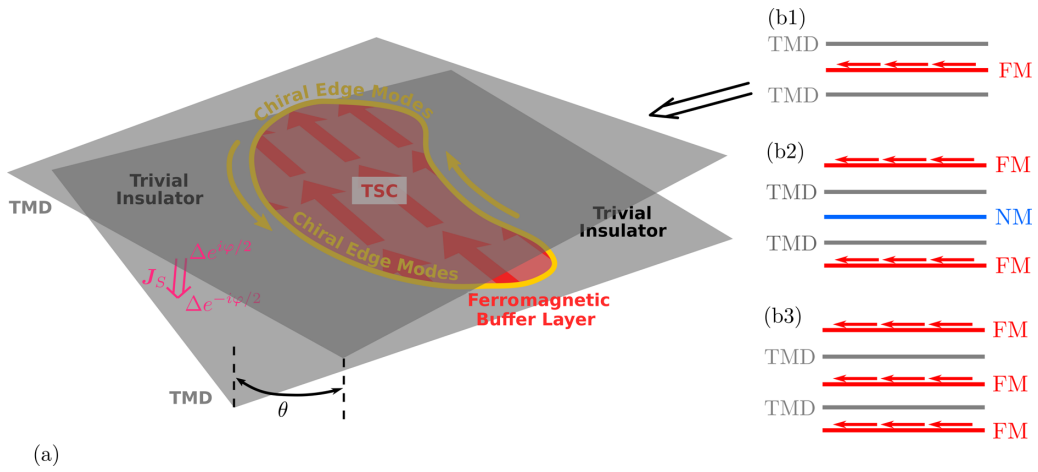


FIG. 1. Setups: proposals of twisted β -bilayer TMD heterostructures with an insulating middle buffer layer. (a) and (b1) Trilayer proposal with a ferromagnetic buffer: (a) shows the proposal in (b1) from a different view. The vertical pink arrow represents the supercurrent J_S tuning the Josephson phase between top and bottom layers of the TMD, and θ is a small twisting angle. The middle buffer layer with an *in-plane* ferromagnetic moment (red arrows) introduces an exchange Zeeman field H_{exch} for TMD layers through the magnetic proximity effect, realizing the chiral topological superconducting phase. Outside the trilayer overlapping region, trivial superconductivity is realized. The gapless chiral edge modes are localized (yellow curves and arrows) at the boundary of the overlapping region. (b2) and (b3) Two additional proposals in the same spirit allowing more tunabilities for the parameters t_{\perp} , $t_{s,\perp}$ and H_{exch} . FM (NM), ferromagnetic (nonmagnetic) buffer layer; TSC, topological superconductivity.

ferromagnetic buffer layer, as shown in Fig. 1. These Zeeman-field-induced nodes were first pointed out theoretically by He *et al.* [30], and experimental evidence for such nodal states in the presence of an external magnetic field has been reported [9,31–33].

Unlike the proposal based on cuprates [24,25], here the topological superconductivity in TMD twisted bilayers is limited to low temperatures $\lesssim 1$ K. Nevertheless, it is worth mentioning a few advantages of the present proposal. First, different from strongly correlated cuprates, the TMD Ising superconductivity has been fairly well understood as conventional *s* – wave pairing without strong correlations. Namely, the low-energy physics of TMDs are well under control in terms of theoretical modeling. Second, detecting the chiral Majorana edge modes is the smoking-gun experiment to identify chiral topological superconductivity. In the present proposal, these edge modes are sharply located at the edge of the ferromagnetic buffer layer and can be detected using either thermal transport or scanning tunneling microscopy (STM) (see Fig. 1 for an illustration). In the proposal based on cuprates, these edge modes will hybridize with the nodal superconductivity due to the irregular shape of the atomically thin flakes and could be challenging to locate in real space.

II. MAIN RESULTS

Unlike twisted bilayer graphene, twisted heterostructures of TMDs have two distinct configurations that differ by a 180° relative rotation, which are referred to as α and β [34]. The α bilayer can be viewed as the building block for the bulk $2H$ -TMD structure, which restores the inversion symmetry. In this paper we instead focus on the β -bilayer structure of Ising superconductors with Fermi pockets around the Γ point (e.g., $2H$ -NbSe₂ and $2H$ -TaS₂ but not gated $2H$ -MoS₂). In addition, a ferromagnetic insulating buffer layer with an *in-plane* mag-

netic moment is placed in the middle of the β bilayer. At small twisting angles between the top and bottom TMD monolayers, we show that the system hosts chiral topological superconductivity when an out-of-plane supercurrent is present (see Fig. 1 for an illustration).

Experimentally, most ferromagnetic vdW materials have an out-of-plane magnetic anisotropy. Only recently has monolayer CrCl₃ been successfully isolated and confirmed to have an *in-plane* ferromagnetic order [12,35]. On the other hand, theoretical first-principles calculations predicted that monolayer Cr₂I₃Cl₃ [36], $2H$ -VS₂ [37], and $2H$ -VSe₂ [38,39] should be insulators with *in-plane* ferromagnetic order. In addition, because of a weak magnetic anisotropy, the ferromagnetic moment in CrBr₃ can be reoriented to an *in-plane* direction by a fairly small external magnetic field (~ 0.5 T) [40]. These vdW materials may serve as the ferromagnetic buffer layer in the present proposal.

Apart from the intrinsic electronic structures of the monolayer TMD, the proposed heterostructures are characterized by three parameters: the Zeeman exchange field H_{exch} induced by the magnetic proximity effect, the *spin-independent* interlayer hopping t_{\perp} , and the *spin-dependent* interlayer hopping $t_{s,\perp}$ (see below). These parameters depend on the choice of the buffer layer in the setup proposed in Figs. 1(a) and 1(b1). Moreover, one may consider more sophisticated multilayer setups as shown in Figs. 1(b2) and 1(b3). By choosing different setups, in principle all of the three parameters can be tuned individually.

In the simplest setup in Figs. 1(a) and 1(b1), H_{exch} and $t_{s,\perp}$ both are originated from the ferromagnetic buffer layer. In general there is no direct relation between them. However, in a mean-field treatment, the second-order perturbation theory gives $t_{s,\perp} = \mu_B H_{\text{exch}}$ (see Appendix B). Although there are no available experimental data to quantify H_{exch} for the proposed heterostructures, similar heterostructures such as WSe₂/CrI₃

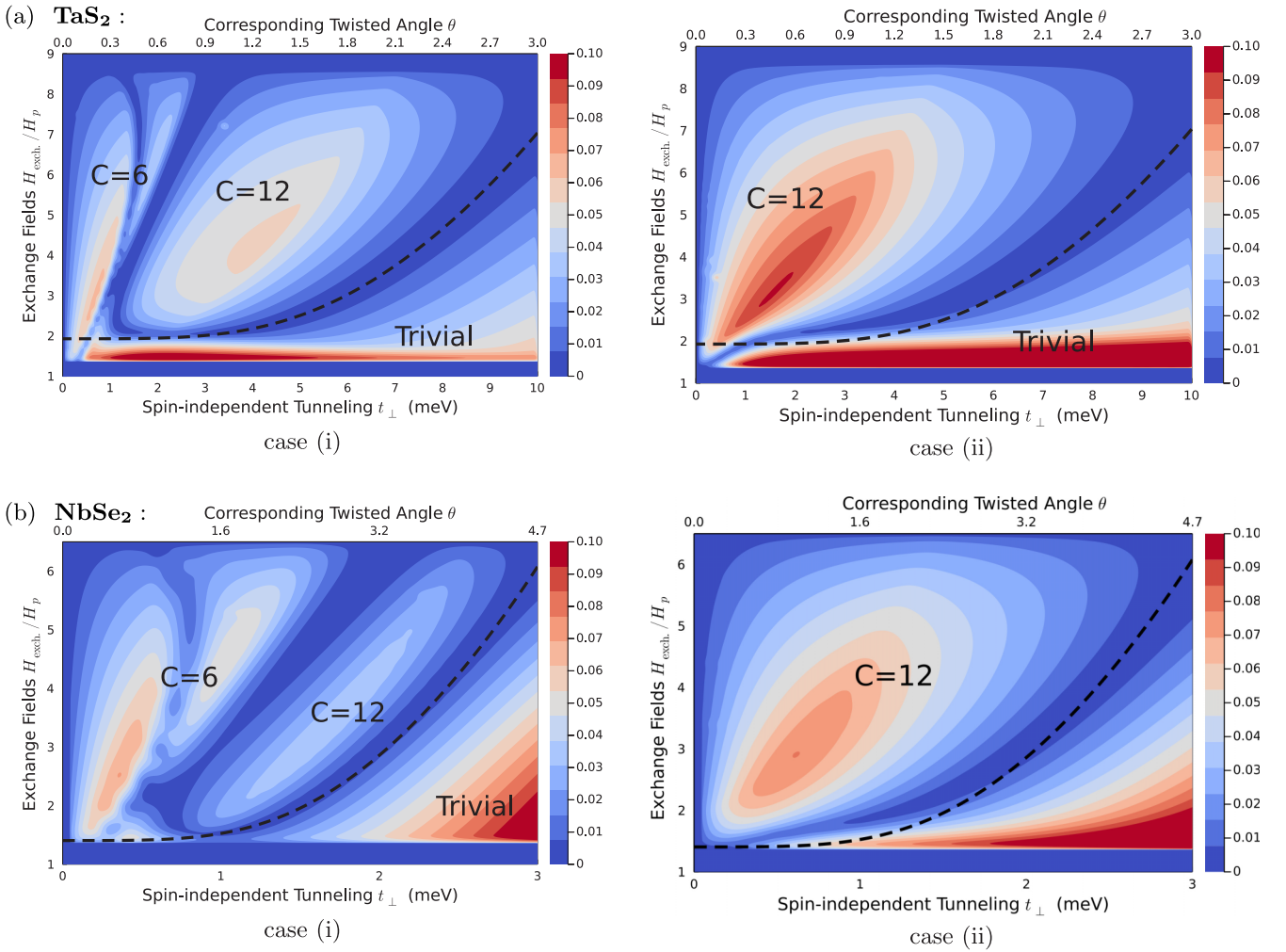


FIG. 2. t_{\perp} - (H/H_p) phase diagram. The superconducting gap (gap minimum in the momentum space) and Chern numbers for proposed heterostructures involving TaS₂ (a) and NbSe₂ (b) based on numerical calculations. Here, the Josephson phase is fixed to be $\varphi = \pi/2$, and the parameter ξ [see Eq. (1) for its definition] is fixed to be $\xi^{\text{TaS}_2} = 0.9$ and $\xi^{\text{NbSe}_2} = 1.1$. H_p in the vertical axis is the Pauli limit field strength. t_{\perp} and the corresponding twisting angle are displayed on the horizontal axis. For both materials the phase diagrams corresponding to case (i) and case (ii) in Eq. (2) are calculated. The black dashed lines exhibit the predicted topological-trivial phase boundary from analytical perturbative calculations [see Eq. (12)].

and MoSe₂/CrBr₃ with an out-of-plane ferromagnetic layer have been well characterized experimentally and theoretically [40–45], where a proximity-induced Zeeman splitting at ~ 1 – 2 meV is reported for electronic bands near the K point. A similar value of splitting in the proposed heterostructures corresponds to $H_{\text{exch}} \approx (3\text{--}6)H_p$, with H_p being the Pauli limit. Notice that monolayer NbSe₂ has been reported to sustain an in-plane upper critical field of $\sim (6\text{--}8)H_p$ [9,31,32] (and $\sim (9\text{--}10)H_p$ for TaS₂ [33,46]).

By means of analytic estimation of the size of topological gaps with the presence of supercurrents [see Eq. (11)], we find that the topological phase is robust at least when a small twisting angle θ is comparable to the fraction $t_{\perp}/(\hbar v_{\text{Ising}} k_F)$, where k_F is the Fermi wave vector and the velocity v_{Ising} is characterizing the Ising SOC near the Γ - M direction [see Eq. (4)]. It turns out to be convenient to introduce a dimensionless parameter to capture the ratio of the two quantities:

$$\xi \equiv \arctan \frac{2t_{\perp}}{\hbar v_{\text{Ising}} k_F \theta}. \quad (1)$$

The proposed setup in Figs. 1(a) and 1(b1) is applied to the heterostructures involving either TaS₂ or NbSe₂. Their monolayer electronic structures are obtained using a relaxed crystal structure based on first-principles calculations (see Appendix C for details). For each TMD material, two cases for the spin-dependent hopping $t_{s,\perp}$ are investigated, corresponding to

$$\text{Case (i): } t_{s,\perp} = \mu_B H_{\text{exch}}, \quad \text{Case (ii): } t_{s,\perp} = 0. \quad (2)$$

We show the global phase diagram by tuning the spin-independent hopping t_{\perp} and the Zeeman exchange field H_{exch} in Fig. 2, based on numerical calculations. For presentation purposes, we have fixed $\xi^{\text{TaS}_2} = 0.9$ and $\xi^{\text{NbSe}_2} = 1.1$ and fixed the Josephson phase $\varphi = \pi/2$ corresponding to the maximal superconducting state. The results are listed as follows.

(a) Topological superconducting phases are found to exist when $t_{\perp} \lesssim 9$ meV for TaS₂ (and $t_{\perp} \lesssim 2.7$ meV for NbSe₂).

(b) A Chern-number-12 phase is found to occupy a large portion of the parameter space, while a Chern-number-6 phase

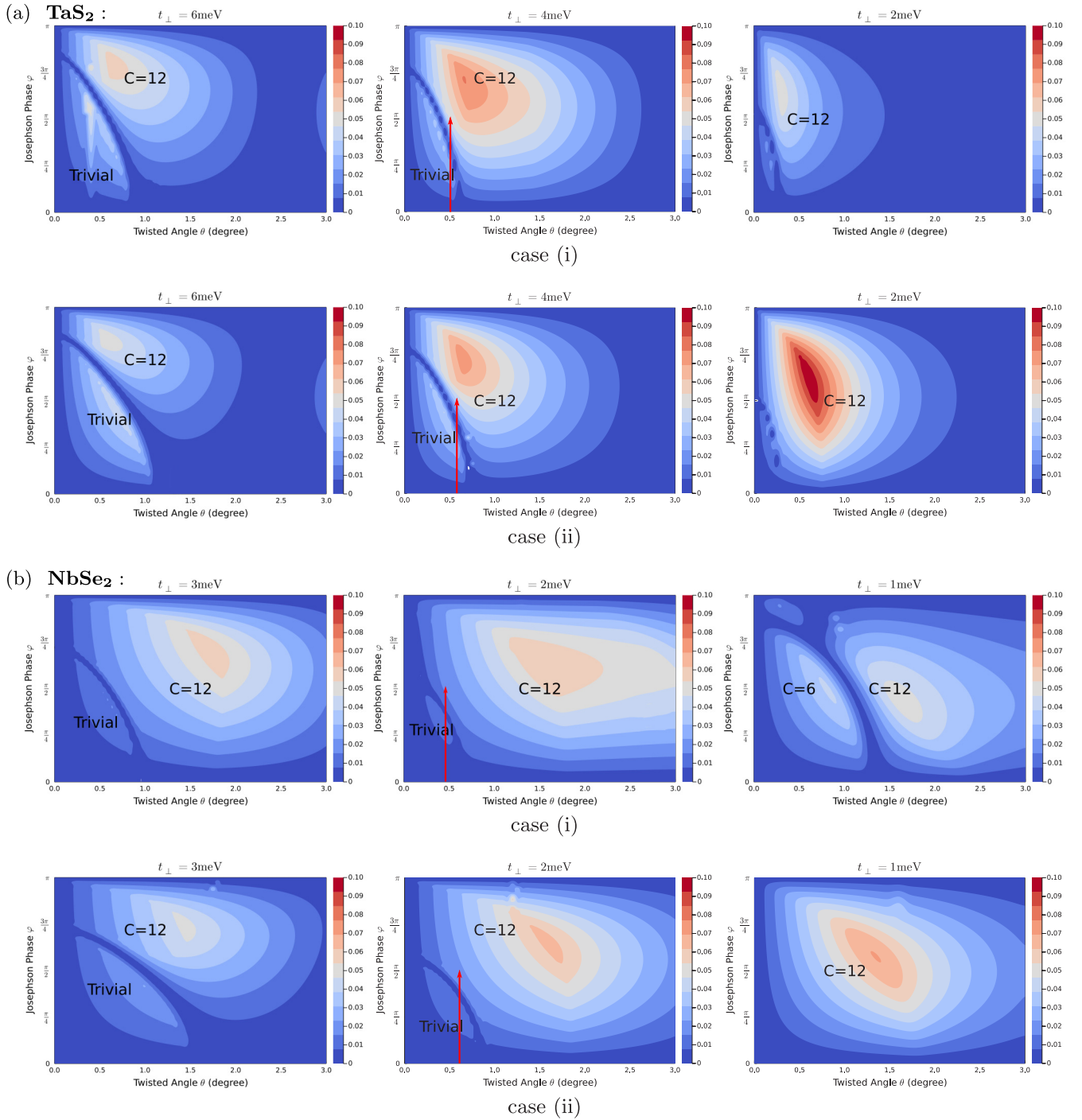


FIG. 3. θ - φ phase diagram. The superconducting gap (gap minimum in the momentum space) and Chern numbers induced by varying the twisting angle θ and the Josephson phase φ for proposed heterostructures involving TaS₂ (a) and NbSe₂ (b). Here, in each panel we fix the Zeeman field to be four times the Pauli limit $H_{\text{exch}} = 4H_p$ and fix the spin-independent tunneling t_{\perp} . Red arrows indicate the trivial-topological phase transitions induced by tuning φ in a single device. Note that the regime $\varphi \leq \pi/2$ corresponds to the stable branch of the Josephson junction.

only appears for case (i) at small values of spin-independent tunneling t_{\perp} .

(c) Under appropriate conditions, the gap in the topological phase can reach 0.1 meV.

The large values of Chern numbers are due to the underlying C_{3z} -rotation symmetry, and these phase diagrams are well understood via analytical calculations. The origin

of the Chern-number-12 phase is due to the topological mass terms generated at 12 Dirac nodes (three groups of four Dirac nodes related by C_{3z} rotation) after the vertical Josephson supercurrent is introduced. In the regime where the Chern-number-6 phase is realized, however, it turns out that topological mass terms are generated only at six Dirac nodes (three groups of two Dirac nodes related by C_{3z} rotation).

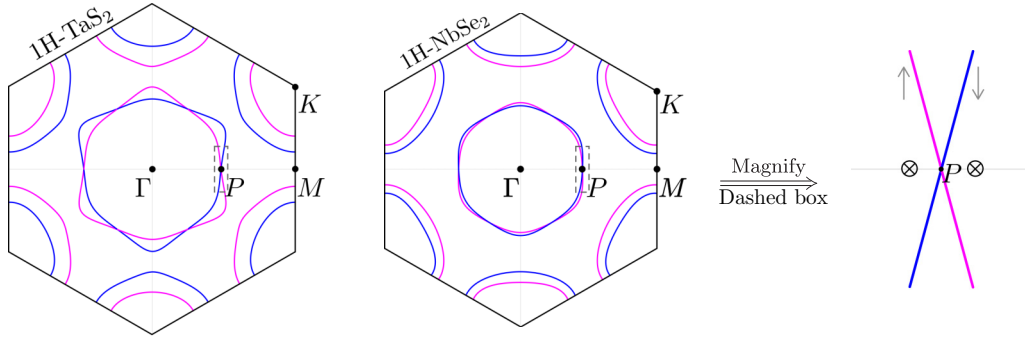


FIG. 4. Monolayer Fermi surfaces and band structures. The Γ pocket and K pocket of monolayer NbSe₂ and TaS₂ are shown. Point P is the intersection of the Γ - M line and the Γ pocket, where Ising SOC vanishes and two nodes (circles with crosses) emerge when an in-plane Zeeman field H_{exch} exceeds the superconducting gap. Magenta and blue colors indicate the different S_z -spin components.

We also plot the phase boundary [see Eq. (12)] between trivial and topological phases from our perturbative calculations in Fig. 2, which is in good agreement with the numerical calculations.

Apart from the global phase diagrams, we also plot the phase diagrams with a few selected values of t_{\perp} . Fixing $H_{\text{exch}} = 4H_p$, we tune the twisting angle θ and the Josephson phase φ , and the results are shown in Fig. 3. Consistent with the global phase diagram, the topological phase is realized when t_{\perp} is not too large. Interestingly, for intermediate values of t_{\perp} , trivial to topological phase transitions are observed by tuning φ alone while fixing the twisting angle θ in an appropriate regime. Such a Josephson-phase-driven topological transition in a single device can lead to unique features to unambiguously identify the topological phase in experiments. For instance, the gapless chiral Majorana edge modes should appear only in the topological phase, after the phase transition occurs when φ is tuned up.

III. MODEL

A. Γ pocket

The bands forming the Γ pockets of monolayer TMD are known to have significant contributions from the d_{z^2} orbital of the transition metal [47]. In the band basis, the minimal effective Hamiltonian takes the form

$$h^{\Gamma}(\mathbf{k}) = \varepsilon_0(\mathbf{k}) + \lambda_{\text{SO}}^{\text{Ising}}(\mathbf{k})\sigma_z, \quad (3)$$

where Pauli σ_i matrices label the spin space, $\varepsilon_0(\mathbf{k})$ represents the kinetic energy, and $\lambda_{\text{SO}}^{\text{Ising}}(\mathbf{k})$ represents the Ising SOC. Drastically different from the usual Rashba SOC, here the Ising SOC $\lambda_{\text{SO}}^{\text{Ising}}(\mathbf{k})$ splits bands with fixed S_z spin. In fact, due to the $z \rightarrow -z$ mirror symmetry of monolayer $2H$ TMDs, the Rashba SOC is forbidden. Time-reversal symmetry dictates that $\lambda_{\text{SO}}^{\text{Ising}}(\mathbf{k}) = -\lambda_{\text{SO}}^{\text{Ising}}(-\mathbf{k})$, so $\lambda_{\text{SO}}^{\text{Ising}}(\mathbf{k})$ necessarily has sign changes. Due to the mirror plane containing the Γ - M axis, the six Γ - M directions are exact where $\lambda_{\text{SO}}^{\text{Ising}}(\mathbf{k})$ changes sign.

We are then able to write down the first-order $\mathbf{k} \cdot \mathbf{p}$ model near the intersection point P between the Fermi surface and one Γ - M direction (the k_x direction; see Fig. 4 for an illustration):

$$h_p^{\Gamma} = \hbar v_F k_x + \hbar v_{\text{Ising}} k_y \sigma_z, \quad (4)$$

where $\lambda_{\text{SO}}^{\text{Ising}}(\mathbf{k})$ vanishes along the k_x direction and $v_{\text{Ising}} \equiv \frac{\partial \lambda_{\text{SO}}^{\text{Ising}}(\mathbf{k})}{\hbar \partial k_y}$. Effective Hamiltonian equation (4) is the starting point of our theory. We list these parameters for NbSe₂ and TaS₂ in Table I based on first-principles calculations (the band structures are plotted in Fig. 5, and the full list of the quartic $\mathbf{k} \cdot \mathbf{p}$ expansion parameters is given in Appendix C).

B. Monolayer

Now let us turn on the Zeeman field H_y along the y direction (the g factor is assumed to be 2) and introduce a spin-singlet pairing Δ [48]. In the Nambu basis, the BCS mean-field Hamiltonian from Eq. (4) reads

$$h_{\text{BCS}}^{\text{mono}} = \hbar v_F k_x \tau_z + \hbar v_{\text{Ising}} k_y \sigma_z + \mu_B H_y \sigma_y + \Delta \sigma_y \tau_y, \quad (5)$$

where Pauli τ matrices label the particle-hole space. Because the system has a spin-rotation symmetry around the S_z direction, the choice of the direction of the in-plane magnetic field is not important. Since there are three independent Γ - M directions, related by C_3 rotations, the full electronic structure of NbSe₂ (TaS₂) has three copies of the effective theory in Eq. (5). The eigenvalues of Eq. (5) can be solved straightforwardly along the Γ - M direction: $\varepsilon_k = \mu_B H_y \pm \sqrt{(v_F k_x)^2 + \Delta^2}$. Clearly, one pair of Dirac nodes will be formed when $\mu_B H_y > \Delta$, located at $k_x = \pm \frac{\hbar v_F}{\mu_B H_y} \sqrt{(\mu_B H_y)^2 - \Delta^2}$ (see Fig. 4 for a schematic illustration), which is consistent with earlier works [29,30]. The low-energy effective theories for either node can also be obtained (in the band basis):

$$h_{\text{node}}^{\pm} = \pm \hbar v_F \cos \eta \cdot \delta k_x \Sigma_z + \hbar v_{\text{Ising}} \sin \eta \cdot \delta k_y \Sigma_x, \quad (6)$$

where $\eta = \arcsin \frac{\Delta}{\mu_B H_y}$, momentum shift $\delta \mathbf{k}$ is measured from the nodal points \mathbf{k}^{\pm} , and Σ_i are Pauli matrices within the low-energy two-dimensional Nambu space.

TABLE I. The parameters in the $\mathbf{k} \cdot \mathbf{p}$ model.

TMD	$\hbar v_F$ (eV Å)	$\hbar v_{\text{Ising}}$ (eV Å)	k_F (Å ⁻¹)	Δ (meV)
NbSe ₂	-2.22	0.12	0.48	0.46
TaS ₂	-2.89	0.36	0.54	0.52

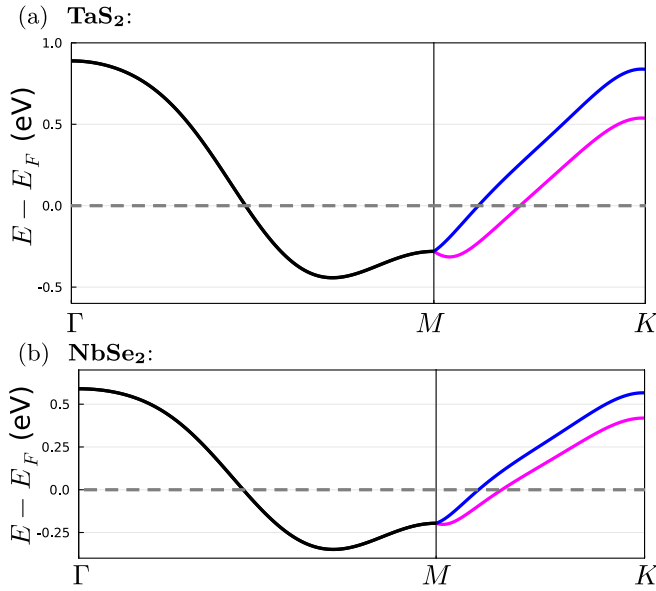


FIG. 5. (a) and (b) Monolayer band structures.

These nodes are protected by a chiral symmetry $\sigma_x \tau_y$ in model equation (5) sending $h(\mathbf{k}) \rightarrow -h(\mathbf{k})$, which corresponds to the combination of the physical time-reversal transformation $i\sigma_y K$, the particle-hole transformation $\tau_x K$, and a S_z - π rotation $i\sigma_z \tau_z$. The existence of the nodes around intersection point P is essential for the topological phase transition induced by a vertical Josephson current in the proposed heterostructures.

C. Twisted bilayer

Next we consider a β bilayer (separated by an insulator buffer layer) with a twisting angle θ , which can be viewed as the top (bottom) monolayer being twisted by angle $\theta/2$ ($-\theta/2$). Introducing k_F as the crystal momentum of point P , we obtain the following effective theory near P :

$$\begin{aligned} h_{\text{BCS}}^{\text{bilayer}} = & \hbar v_F k_x \tau_z + \hbar v_{\text{Ising}} k_y \sigma_z + \Delta \cos \frac{\varphi}{2} \sigma_y \tau_y \\ & + \Delta \sin \frac{\varphi}{2} \sigma_y \tau_x \nu_z - \hbar v_{\text{Ising}} k_F \frac{\theta}{2} \sigma_z \nu_z + \mu_B H_y \sigma_y \\ & + t_{\perp} \tau_z \nu_x + t_{s_y, \perp} \sigma_y \nu_x. \end{aligned} \quad (7)$$

Here, the Pauli matrices ν capture the top and bottom layer space. $\Delta > 0$, and the pairing amplitude is $\Delta e^{i\varphi/2}$ ($\Delta e^{-i\varphi/2}$) for the top (bottom) layer. The t_{\perp} and $t_{s_y, \perp}$ terms describe the spin-independent and spin-dependent interlayer hopping processes, respectively. Based on the two-center approximation [19,21], and the fact that point P is far away from the Brillouin zone boundary, the interlayer hopping processes have a weak stacking dependence and are considered as constants in this paper [27,28] (see Appendix E for a discussion of the two-center approximation).

The model equation (7) can be analytically solved in various perturbative regimes. To demonstrate the stability of the topological superconductivity, below we focus on one particular regime, in which $\sqrt{(\hbar v_{\text{Ising}} k_F \theta)^2 + 4t_{\perp}^2} \gg \Delta, \mu_B H_y, t_{s_y, \perp}$. The advantage of this regime is that it is always realizable in

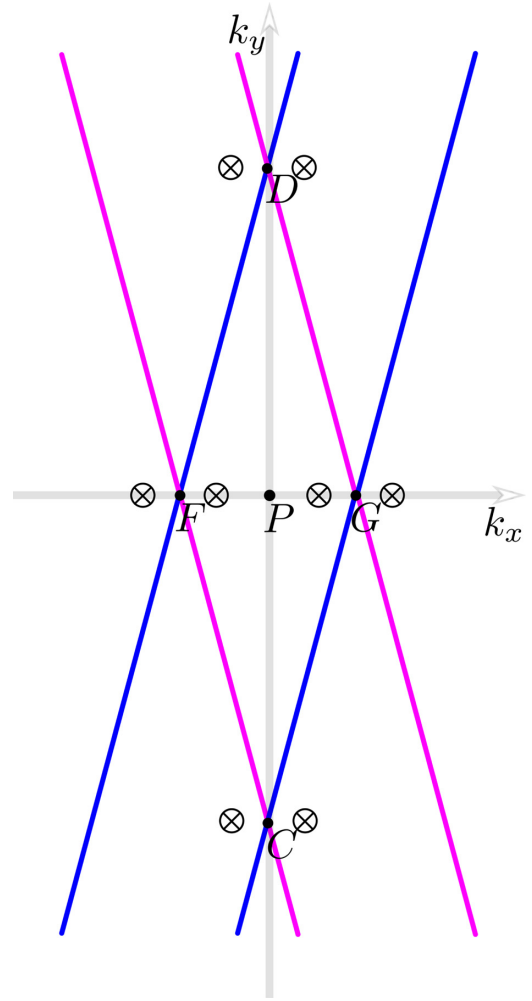


FIG. 6. Schematic plot of four Fermi surface intersection points in a twisted bilayer near point P . Four Fermi surfaces are linearized for small twisting angle. When $\varphi = 0$, each intersection point will give rise to two pairing nodes after H_{exch} is tuned up. When $\varphi \neq 0$, these nodes open up energy gaps: The four nodes near points F and G along the Γ - M line have a total Chern number of zero. The four nodes near points C and D have a total Chern number of 4.

the proposed heterostructures by tuning the twisting angle θ . In this regime, we find that the topological superconductivity with Chern number 4 (corresponding to Chern number 12 for the whole heterostructure) is always realized in model equation (7) by tuning φ, θ and $\mu_B H_y \gtrsim \Delta$.

To understand this behavior, we may first turn off the pairing Δ and $\mu_B H_y, t_{s_y, \perp}$ in model equation (7). There are four intersection points between the spin-up and spin-down Fermi surfaces, which we label as C, D and F, G and which are located at the k_y and k_x axes, respectively (see Fig. 6). The low-energy effective theory near each point resembles Eq. (4) with modified v_F and v_{Ising} .

After Δ, φ are turned on but $\mu_B H_y = t_{s_y, \perp} = 0$, the pairing gap minima near $C, D, F,$ and G are found to be the same: $\Delta_{C,D,F,G} = \Delta \sqrt{\cos^2 \frac{\varphi}{2} + \cos^2 \xi \sin^2 \frac{\varphi}{2}}$, where ξ is defined in Eq. (1). Because of the connection with the $\varphi = 0$ limit, the superconducting phase so far must still be topologically trivial even though $\varphi \neq 0$ breaks the time-reversal symmetry.

When $\mu_B H_y, t_{s_y, \perp} \neq 0$ are tuned up, the behavior near points C and D and that near points F and G are qualitatively different. The pairing gap minima near F and G never go to zero as long as $\varphi \neq 0$. In particular, we find

$$\Delta_{F,G} = \begin{cases} \sqrt{(\Delta \cos \frac{\varphi}{2} - b)^2 + \Delta^2 \cos^2 \xi \sin^2 \frac{\varphi}{2}}, & b < \Delta \cos \frac{\varphi}{2} \\ \Delta \cos \xi |\sin \frac{\varphi}{2}|, & b \geq \Delta \cos \frac{\varphi}{2}, \end{cases} \quad (8)$$

where

$$b \equiv \begin{cases} |\mu_B H_y \sin \xi - t_{s_y, \perp}| & \text{for point } F \\ |\mu_B H_y \sin \xi + t_{s_y, \perp}| & \text{for point } G. \end{cases} \quad (9)$$

In contrast, near points C and D the topological phase transition occurs with four Dirac nodes (two near each point) emerging when $H_y = H_c^{\text{topo}}$, where the critical Zeeman field strength is

$$\mu_B H_c^{\text{topo}} \equiv \Delta \sqrt{\sec^2 \xi \cos^2 \frac{\varphi}{2} + \sin^2 \frac{\varphi}{2}}. \quad (10)$$

When $H_y > H_c^{\text{topo}}$, the four Dirac nodes acquire a topological mass gap, transferring a Chern number of 4:

$$\Delta_{C,D}^{\text{topo}} = \sin \varphi \frac{\Delta^2 \sin^2 \xi}{\hbar v_{\text{Ising}} k_F \theta} \sqrt{\left(\frac{H_y}{H_c^{\text{topo}}}\right)^2 - 1}. \quad (11)$$

The details of the calculations are presented in Appendix D.

Note that different from $\Delta_{F,G}$, the topological gap $\Delta_{C,D}^{\text{topo}} \propto \Delta^2$. This is because the Δ -linear-order gap remains zero in the present linear-order $\mathbf{k} \cdot \mathbf{p}$ effective theory, and the second-order perturbation plays the dominant role: The topological phase is always realized when $H_y > H_c^{\text{topo}}$.

When a higher-order $\mathbf{k} \cdot \mathbf{p}$ expansion is considered, we do find that a nontopological Δ -linear-order gap near C and D becomes nonzero (see Appendix D). When this gap is large, the topological superconductivity will be destroyed. Based on perturbative calculations, the topological phase requires the following criterion to be satisfied [see Appendix D, Eq. (D25), for details]:

$$t_{\perp}^2 < \frac{\Delta \hbar k_F v_{\text{Ising}}^2}{v_2} a(\xi, \varphi) \sqrt{\left(\frac{H_y}{H_c^{\text{topo}}}\right)^2 - 1},$$

$$a(\xi, \varphi) \equiv \tan \xi \sin \xi \sqrt{\sec^2 \xi \cos^2 \frac{\varphi}{2} + \sin^2 \frac{\varphi}{2}}. \quad (12)$$

Here, v_2 is a velocity parameter [defined in Eq. (D3)] in the quadratic-order $\mathbf{k} \cdot \mathbf{p}$ expansion, and $\hbar v_2^{\text{NbSe}_2} = 0.94 \text{ eV \AA}$ and $\hbar v_2^{\text{TaS}_2} = 3.1 \text{ eV \AA}$ based on our electronic structure calculations (see Appendix C). Namely, t_{\perp} cannot be too large. This criterion serves as the phase boundary between the trivial and topological phases and is plotted in Fig. 2 as the dashed black line.

The previous perturbative regime well captures the Chern-number-12 topological phase. Aiming at understanding the Chern-number-6 topological phase in the numerical phase diagrams, we have performed the analytical calculations in a different perturbative regime, $t_{\perp} \ll \Delta$, $\hbar v_{\text{Ising}} k_F \theta \ll \Delta$, and reproduced the Chern-number-6 topological phase (see Appendix D).

IV. DISCUSSION AND CONCLUSIONS

Before concluding, we would like to remark on a few experiment-related issues:

Chiral edge modes. When topological superconductivity is realized in the proposed heterostructure in Figs. 1(a) and 1(b1), the edge of the ferromagnetic buffer layer is the natural boundary between the topological superconductivity and trivial superconductivity. This is because outside the buffer layer region, due to the lack of Zeeman exchange field, gapped trivial superconductivity is realized in the TMD bilayer. Majorana chiral edge modes are then sharply located at this edge, leading to the well-known quantized thermal Hall conductance $\frac{\kappa_{xy}}{T} = C \frac{\pi}{12} \frac{k_B^2}{\hbar}$, where C is the Chern number. In addition, the edge modes can be detected via scanning tunneling microscopy as midgap states.

Midgap states located at the edge of a superconducting material may also have nontopological explanations, such as the Yu-Shiba-Rusinov bound states. However, in an appropriate regime, as shown in Fig. 3, we note that a single device may realize a trivial to topological phase transition while the Josephson phase φ is tuned up. Such a φ -driven topological phase transition has unique experimental signatures since the Majorana edge states are expected to exist only in the topological phase, which may be used to sharply identify the nature of the midgap states.

The effect of an in-plane external magnetic field. When an in-plane magnetic field is applied to the proposed heterostructures, the Josephson phase $\varphi(x) = 2\pi x/L$ becomes spatially dependent along the in-plane transverse direction, where $L = \frac{\Phi_0}{H_{\text{ext}} d}$ and d is the effective thickness of the junction. For instance, an external magnetic field $H_{\text{ext}} \sim 0.5 \text{ T}$ is needed to reorient the magnetic moment of CrBr_3 to an in-plane direction, corresponding to $L \sim 2 \mu\text{m}$ if $d \sim 20 \text{ \AA}$ is used. Due to the fact that the Chern number flips sign when $\varphi \rightarrow -\varphi$, the topological superconductivity is expected to form spatial stripes, or domains with width $L/2$, with alternating Chern numbers, e.g., $C = \pm 12$, in which case 24 chiral Majorana states are expected to form at each domain wall. In Appendix A we estimate the spatial spread l_{\perp} of the domain-wall Majorana states along the transverse direction of the domain wall. Only when the spatial spread l_{\perp} is much smaller than the stripe width $L/2$ are the domain-wall states well defined. We find that for a generic magnetic field direction, l_{\perp} is comparable to $L/2$ for $H_{\text{ext}} \sim 0.5 \text{ T}$. However, when H_{ext} is parallel to one Γ - M direction, eight among the 24 domain-wall Majorana states have an l_{\perp} that can be ~ 5 – 10 times smaller than $L/2$. These domain-wall chiral states may be observable in probes such as STM or thermal transport.

Charge-density-wave order. It is known that Ising superconductivity in $2H$ -NbSe₂ or $2H$ -TaS₂ coexists with the charge-density-wave (CDW) order [49–51]. For the Fermi pockets around Γ , the Fermi surface folding due to the CDW occurs near the Γ - K direction. Such behavior would not qualitatively affect the low-energy physics near the Γ - M direction, which is the focus of this paper.

Rashba spin-orbit coupling. As emphasized before, the $z \rightarrow -z$ mirror symmetry forbids the Rashba SOC in the monolayer TMD. A Rashba SOC breaks an important

invariance of Eq. (7) related to the combination of particle-hole and time-reversal transformation $\text{PH} \circ \text{TR} = \sigma_y \tau_x$. $\text{PH} \circ \text{TR}$ always sends $h_{\text{BCS}}^{\text{bilayer}}(\mathbf{k}, H_y, \varphi) \mapsto -h_{\text{BCS}}^{\text{bilayer}}(\mathbf{k}, -H_y, -\varphi)$. In the absence of the Rashba SOC, one may flip the sign of H_y and φ by a complex conjugation since all other terms in the Hamiltonian are real: $-h_{\text{BCS}}^{\text{bilayer}}(\mathbf{k}, -H_y, -\varphi) = -(h_{\text{BCS}}^{\text{bilayer}})^*(\mathbf{k}, H_y, \varphi)$. Namely, there is an invariance protecting the Bogoliubov quasiparticle spectrum being $\pm E$ symmetric at any \mathbf{k} . Such an invariance is lost in the presence of a Rashba SOC, leading to Bogoliubov Fermi pockets [29].

In the proposed heterostructures, despite the lack of the $z \rightarrow -z$ mirror symmetry, the intrinsic Rashba coupling induced by the vdW interlayer interactions can be safely neglected since it is extremely weak (see Appendix C). Although an extrinsic, substrate-induced Rashba coupling is possible, in this paper we do not consider this effect, since nevertheless this coupling could be tuned to zero via gating.

Interlayer tunneling strength. It is clear from the phase diagrams in Fig. 2 and criterion equation (12) that the interlayer tunneling t_{\perp} cannot be too large in order to realize the topological superconductivity (< 10 meV). On the other hand, based on our density functional theory (DFT) calculations (see Appendix C), due to the d_{z^2} nature of Fermi pockets around the Γ point, a fairly large interlayer tunneling of the bilayer systems of NbSe₂ or TaS₂ without a buffer layer is found near point P (> 50 meV) [52]. This actually motivates us to consider the insulating buffer layer in the proposed heterostructures. In Appendix C, as an estimate, we performed DFT calculations on a TaS₂/WS₂/TaS₂ heterostructure, and $t_{\perp} \sim 5$ meV is found—well within the regime where topological superconductivity is realized.

In summary, we theoretically propose twisted bilayer vdW Ising superconductors as a flexible and tunable platform to realize chiral topological superconductivity with Chern numbers. In the simplest setup, an insulating buffer layer with an in-plane ferromagnetic moment is introduced between TMD Ising superconductors such as NbSe₂ or TaS₂, providing a Zeeman exchange field in the TMD layers via the magnetic proximity effect. We show that the out-of-plane supercurrent induces topological superconductivity over a large parameter regime, and the characteristic Majorana chiral edge modes are localized on the edge of the ferromagnetic buffer layer. We hope that the present study may motivate further experimental and theoretical investigations of such vdW heterostructures.

ACKNOWLEDGMENTS

Y.R. and X.H. acknowledge support from the National Science Foundation under Grant No. DMR-1712128. We thank Di Xiao for helpful discussions. X.H. is thankful for the open discussion of distributive computation on JULIA Discourse and for the high-performance computing (HPC) resources of the Andromeda cluster at Boston College.

APPENDIX A: DOMAIN-WALL CHIRAL MODES

Assuming internode scattering to be weak, here we may use the Dirac equation for a single node to estimate the spatial

size of the chiral domain-wall modes. Denoting the magnetic field direction as \hat{B} , we have the spatial-dependent Josephson phase $\varphi(\mathbf{r}) = \frac{2\pi}{L} \hat{B} \times \hat{z} \cdot \mathbf{r} \equiv \frac{2\pi}{L} \hat{n} \cdot \mathbf{r}$, where we defined unit vector $\hat{n} \equiv \hat{B} \times \hat{z}$. Based on Eq. (11), the spatial-dependent Dirac equation becomes

$$H = v_x p_x \Sigma_x + v_y p_y \Sigma_z + m_0 \sin \varphi(\mathbf{r}) \Sigma_y, \quad (\text{A1})$$

where

$$m_0 \equiv \frac{\Delta^2 \sin^2 \xi}{\hbar v_{\text{Ising}} k_F \theta} \sqrt{\left(\frac{H_y}{H_c^{\text{topo}}}\right)^2 - 1}. \quad (\text{A2})$$

$v_x = v_F \cos \theta^+$ and $v_y = v_{\text{Ising}} \sin \theta^+$ according to Eq. (D19), and $v_x \gg v_y$ since θ^+ is an angle parameter of order unity. The mass-sign-changing domain walls are located at $\hat{n} \cdot \mathbf{r} = \frac{kL}{2}$, and $k \in \mathbb{Z}$. Near each domain wall, we may linearize the mass as $m_0 \sin \varphi(\mathbf{r}) \sim (-1)^k m_0 \tilde{\varphi}(\delta \mathbf{r})$, where $\tilde{\varphi}(\delta \mathbf{r}) = \varphi(\mathbf{r}) - k\pi = \frac{2\pi \hat{n} \cdot \delta \mathbf{r}}{L}$, and $\delta \mathbf{r}$ is the position measured from the domain wall.

It is now convenient to rotate into the coordinate system with axes $(x_{\parallel}, x_{\perp})$ along and perpendicular to the domain wall. The corresponding momenta are denoted as $(p_{\parallel}, p_{\perp})$. Writing the cosine c and sine s of the rotation angle between the two coordinate systems, then $p_x \equiv cp_{\parallel} - sp_{\perp}$ and $p_y \equiv sp_{\parallel} + cp_{\perp}$, and we have

$$H = v_x (cp_{\parallel} - sp_{\perp}) \Sigma_x + v_y (sp_{\parallel} + cp_{\perp}) \Sigma_z + (-1)^k m_0 \frac{2\pi x_{\perp}}{L} \Sigma_y. \quad (\text{A3})$$

H^2 has a simple form:

$$H^2 = v_x^2 (cp_{\parallel} - sp_{\perp})^2 + v_y^2 (sp_{\parallel} + cp_{\perp})^2 + m_0^2 \left(\frac{2\pi x_{\perp}}{L}\right)^2 - (-1)^k \hbar m_0 \frac{2\pi}{L} (sv_x \Sigma_z + cv_y \Sigma_x). \quad (\text{A4})$$

Since p_{\parallel} is a good quantum number, we are left with a one-dimensional harmonic oscillator involving p_{\perp}, x_{\perp} :

$$H^2 = ((cv_x)^2 + (sv_y)^2) p_{\parallel}^2 + ((sv_x)^2 + (cv_y)^2) (p_{\perp} - p_0(p_{\parallel}))^2 + m_0^2 \left(\frac{2\pi x_{\perp}}{L}\right)^2 - (-1)^k \hbar m_0 \frac{2\pi}{L} (sv_x \Sigma_z + cv_y \Sigma_x), \quad (\text{A5})$$

where p_0 is a linear function of p_{\parallel} . The corresponding mass and frequency for this harmonic oscillator are

$$M = \frac{1}{2} [(sv_x)^2 + (cv_y)^2]^{-1}, \quad \omega = \sqrt{2M^{-1}} \frac{m_0 2\pi}{L}. \quad (\text{A6})$$

The energy levels are

$$E_n = 2\hbar \sqrt{(sv_x)^2 + (cv_y)^2} \frac{m_0 2\pi}{L} \left(n + \frac{1}{2}\right). \quad (\text{A7})$$

The zero-energy state of H and H^2 for $p_{\parallel} = 0$, corresponding to the chiral Majorana modes, is the $n = 0$ ground state of the harmonic oscillator. The last term in H^2 chooses a specific eigenstate of $(sv_x \Sigma_z + cv_y \Sigma_x)$, so that the zero-point energy in the harmonic oscillator is exactly canceled. Since we are working with complex fermions, this zero-energy state corresponds to two chiral Majorana modes.

The spatial spread l of the chiral model along the x_{\perp} direction can be readily read out from the harmonic oscillator ground state $\psi(x_{\perp}) \propto e^{-x_{\perp}^2/(2l_{\perp}^2)}$:

$$l_{\perp} = \sqrt{\frac{\hbar}{M\omega}} = \sqrt{\frac{\hbar[(sv_x)^2 + (cv_y)^2]^{1/2}L}{2\pi m_0}}. \quad (\text{A8})$$

l_{\perp} is proportional to the square root of the velocity $[(sv_x)^2 + (cv_y)^2]^{1/2}$. Note that $v_x \gg v_y$; for a generic magnetic field direction, $l_{\perp} \sim \sqrt{\frac{\hbar v_x L}{2\pi m_0}}$. Assuming $\hbar v_x \sim 1$ eV Å, $m_0 \sim 0.1$ meV, and $L \sim 2$ μm, one finds $l_{\perp} \sim 0.4 \cdot L/2$.

To minimize l_{\perp} , one may choose the magnetic field direction (i.e., the domain-wall direction) to be along x (i.e., one Γ - M direction), leading to $l_{\perp} = \sqrt{\frac{\hbar v_x L}{2\pi m_0}}$ for four nodes near this Γ - M direction among the total of 12 nodes. In this case, among the 24 Majorana domain-wall states, eight of them have $l_{\perp} \sim 0.2 \cdot L/2$ (for TaS₂) and $l_{\perp} \sim 0.1 \cdot L/2$ (for NbSe₂) using the parameters above.

APPENDIX B: A MEAN-FIELD TREATMENT FOR THE FERROMAGNETIC BUFFER LAYER

We will show in this Appendix that, for the proposed setup in Figs. 1(a) and 1(b1) with a ferromagnetic buffer layer, the direct couplings between the top or bottom layer and the middle layer will induce an in-plane exchange Zeeman field H_{exch} and a spin-dependent tunneling $t_{s,\perp}$. In a simple perturbative mean-field treatment, $\mu_B H_{\text{exch}} = t_{s,\perp}$.

Without loss of generality, we can work in the basis where the buffer layer Hamiltonian is diagonalized $\mathbf{h}^m = \text{diag}\{h_{\uparrow}^m, h_{\downarrow}^m\}$, where \uparrow and \downarrow indicate the spin components parallel and antiparallel to the *in-plane ferromagnetic moment direction*. For simplicity we assume that h_{\uparrow}^m and h_{\downarrow}^m each contain a single band, which can be easily generalized to multiband cases.

In the absence of the middle layer, we consider the spinful TMD bilayer Hamiltonian $\mathbf{h}^{\text{bilayer}} = \text{diag}\{\mathbf{h}^t(\mathbf{k}), \mathbf{h}^b(\mathbf{k})\}$. The full Hamiltonian for the trilayer system is then

$$H^{\text{trilayer}}(\mathbf{k}) = \left(\begin{array}{cc|cc} \mathbf{h}^t(\mathbf{k}) & & & \mathbf{V} \\ & \mathbf{h}^b(\mathbf{k}) & & \\ \hline & & h_{\uparrow}^m & \\ \mathbf{V}^T & & & h_{\downarrow}^m \end{array} \right), \quad (\text{B1})$$

where $\mathbf{V} = (\mathbf{V}_1, \mathbf{V}_2)$, $\mathbf{V}_1 = (t_{\uparrow}^t, 0, t_{\uparrow}^b, 0)^T$, and $\mathbf{V}_2 = (0, t_{\downarrow}^t, 0, t_{\downarrow}^b)^T$.

Due to the $z \rightarrow -z$ mirror symmetry for the TMD bilayer at the zero twisting angle, one may assume these direct hoppings to be layer independent, $t_{\uparrow,\downarrow}^{t,b} = t_{\uparrow,\downarrow}$, at small twisting angles. Since the middle buffer layer is an insulator, h_{\uparrow}^m and

h_{\downarrow}^m are high-energy states. Standard perturbation theory gives

$$\begin{aligned} H_{\text{induced}}^{\text{bilayer}}(\mathbf{k}) &\simeq \mathbf{h}^{\text{bilayer}} - \sum_{i=1,2} \mathbf{V}_i (\mathbf{h}^m)^{-1} \mathbf{V}_i^T \\ &= \mathbf{h}^{\text{bilayer}} - \frac{t_{\uparrow}^2}{h_{\uparrow}^m} \begin{pmatrix} 1 & 0 & 1 & 0 \\ 0 & 0 & 0 & 0 \\ 1 & 0 & 1 & 0 \\ 0 & 0 & 0 & 0 \end{pmatrix} \\ &\quad - \frac{t_{\downarrow}^2}{h_{\downarrow}^m} \begin{pmatrix} 0 & 0 & 0 & 0 \\ 0 & 1 & 0 & 1 \\ 0 & 0 & 0 & 0 \\ 0 & 1 & 0 & 1 \end{pmatrix} \\ &= \mathbf{h}^{\text{bilayer}} - \delta\mu\sigma_0\nu_0 + t_{\perp}\sigma_0\nu_x + \mu_B H_{\text{exch},z}\sigma_z\nu_0 \\ &\quad + t_{s,\perp}\sigma_z\nu_x, \end{aligned} \quad (\text{B2})$$

where we separate out the second-order perturbation of the bilayer Hamiltonian into four parts: the chemical potential shift $\delta\mu$, the spin-independent tunneling t_{\perp} , the (proximity-induced) Zeeman field H_{exch} , and the spin-dependent tunneling $t_{s,\perp}$, where

$$-\delta\mu = t_{\perp} = -\frac{1}{2} \left(\frac{t_{\uparrow}^2}{h_{\uparrow}^m} + \frac{t_{\downarrow}^2}{h_{\downarrow}^m} \right), \quad (\text{B3})$$

$$\mu_B H_{\text{exch}} = t_{s,\perp} = -\frac{1}{2} \left(\frac{t_{\uparrow}^2}{h_{\uparrow}^m} - \frac{t_{\downarrow}^2}{h_{\downarrow}^m} \right). \quad (\text{B4})$$

APPENDIX C: DETAILS OF THE PHASE DIAGRAM CALCULATIONS AND DISCUSSION OF THE STACKING DEPENDENCE

All phase diagrams of the proposed heterostructures involving either $2H$ -NbSe₂ or $2H$ -TaS₂ are obtained by listing the gap size for all eight nodes (topological and trivial) and picking out the *minima* of them. To capture the physics among entire phase diagrams (particularly the large- H_{exch} regions), we follow Ref. [31] to introduce the pair-breaking equation throughout our numerical calculation

$$\ln(T_c/T_{c0}) + \psi\left(\frac{1}{2} + \frac{\mu_B H^2/H_{\text{so}}}{2\pi k_B T_c}\right) - \psi(1/2) \equiv 0,$$

where ψ is the digamma function, T_{c0} is the zero-field critical temperature (3.0 K for NbSe₂ [31] and 3.4 K for TaS₂ [53]), and H_{so} can be taken as a fitting parameter to match the asymptotic Ginzburg-Landau behavior $H \sim H_0 \sqrt{1 - T/T_{c0}}$ for $T_c \sim T_{c0}$, where $H_0 \sim \sqrt{H_{\text{so}} H_p}$ and the Pauli limit $H_p = \frac{\Delta_0}{\sqrt{2}\mu_B} = (1.86 \text{ T/K}) \cdot T_{c0}$ assuming the g factor to be equal to 2 and the BCS formula $\Delta_0 = 1.76 k_B T_{c0}$ still to hold [54]. The best fitting of the experimental data gives $H_0 = 43.6$ T for NbSe₂ and $H_0 = 65.6$ T for TaS₂ [9], so we take $H_{\text{so}}^{\text{NbSe}_2} = 340$ T and $H_{\text{so}}^{\text{TaS}_2} = 680$ T throughout our numerical calculations.

All parameters that we input in our numerical calculations of phase diagrams (up to the fourth order of the $\mathbf{k} \cdot \mathbf{p}$ expansion) are extracted from the monolayer tight-binding models obtained from local density approximation (LDA) calculations by the QUANTUM ESPRESSO [55,56] and WANNIER90 routines [57]. Our strategy is to first build an AA-stacking β -bilayer slab system for both materials and then relax the

TABLE II. Fitting results for Eq. (C1) for both TaS₂ and NbSe₂ (in the eV Å unit system). We set $\hbar = 1$ so that this table can serve as a complement to Table I.

Material	Coeff. p_i																
	k_F	v_F	a	p_5	p_6	p_7	p_8	p_9	p_{10}	p_{11}	v_{Ising}	p_{13}	p_{14}	p_{15}	p_{16}	p_{17}	
TaS ₂	0.54	-2.89	0.25	2.34	17.82	-8.72	11.53	-8.67	17.20	0.00	0.36	1.41	-1.06	-0.72	-2.11	-8.45	
NbSe ₂	0.48	-2.22	-0.76	1.36	15.10	-2.98	9.85	0.76	26.15	0.00	0.12	0.86	-0.20	0.25	-3.56	-4.14	

structure with nonlocal van der Waals correlation functionals to get the proper layer distance and (spin-independent) tunneling strengths. For convergence reasons, we choose to use the functional vdW-DF-C6 [58,59] for TaS₂, while we use vdW-DF2-C09 [60,61] for NbSe₂. The resulting relaxed layer separation is $d_{\perp}^{\text{TaS}_2} = 6.57$ Å and $d_{\perp}^{\text{NbSe}_2} = 6.80$ Å. Since tunneling processes only occur around the intersection points P , with their strengths being half of the energy splitting around the Fermi energy ε_F , we can directly read them out from the the non-self-consistent output at $\mathbf{k} = (k_F, 0)$, reading $t_{\perp}^{\text{TaS}_2} = 56.9$ meV and $t_{\perp}^{\text{NbSe}_2} = 116.2$ meV.

Next, we take the relaxed structure as an input to build a monolayer slab system and perform a LDA calculation to obtain a monolayer electronic structure. Note that this monolayer relaxed structure weakly breaks the $z \rightarrow -z$ symmetry but preserves the mirror planes parallel with the z axis. The LDA result is used to fit the $\mathbf{k} \cdot \mathbf{p}$ model up to quartic order. More precisely, we fit the model consistent with the $y \rightarrow -y$ mirror symmetry:

$$\begin{aligned}
H_{\text{quartic}}^{\text{mono}}(\mathbf{k}) = & [\varepsilon_F + v_F k_x + a k_y^2 + p_5 k_x^2 + p_6 k_x k_y^2 \\
& + p_7 k_y^4 + p_8 k_x^3 + p_9 k_x^4 + p_{10} k_x^2 k_y^2] \sigma_0 \\
& + p_{11} \sigma_y + [v_{\text{Ising}} k_y + p_{13} k_x k_y + p_{14} k_y^3 \\
& + p_{15} k_x^2 k_y + p_{16} k_x^3 k_y + p_{17} k_x k_y^3] \sigma_z. \quad (\text{C1})
\end{aligned}$$

The results for both TaS₂ and NbSe₂ are listed in Table II. The intrinsic Rashba SOC, ignored in Eq. (4), appears as the vanishingly small p_{11} in the fitting in Table II. Due to the loss of the $z \rightarrow -z$ mirror symmetry in the vdW relaxed structure, in principle this coupling may be nonzero. However, we find that the raw energy splitting (corresponding to $2p_{11}$) at point P is less than 10^{-10} meV for both NbSe₂ and TaS₂ and conclude that weak vdW interactions cannot lead to any sizable intrinsic Rashba SOC.

The values of the aforementioned spin-independent tunnelings t_{\perp} for bilayer NbSe₂ and TaS₂ are far beyond the topological superconducting regime that we find in the numerical phase diagrams. This actually motivates us to propose the buffer layer heterostructures in Fig. 1. To have an estimation of the magnitude of the spin-independent tunneling t_{\perp} after the insertion of an insulating buffer layer, we build a trilayer slab system TaS₂/WS₂/TaS₂ of ABA and AAA stackings. Since $2H$ -TaS₂ and $2H$ -WS₂ have similar lattice constants, we use the lattice constants of $2H$ -TaS₂ for the trilayer system without enlarging the supercell [62] ($a = 0.331$ nm and $c = 0.121$ nm for $2H$ -TaS₂ and $a = 0.315$ nm and $c = 0.121$ nm for $2H$ -WS₂). We then again relax the positions for all atoms of the trilayer system with the nonlocal van der Waals functional vdW-DF-C6 [58,59] along the out-

of-plane direction. We find that after inserting a nonmagnetic buffer layer WS₂, the separation between the top and bottom TaS₂ layers for both stackings almost doubles to $d_{\perp}^{\text{TaS}_2, \text{ABA}} = 12.00$ Å and $d_{\perp}^{\text{TaS}_2, \text{AAA}} = 13.18$ Å, and the corresponding strengths of the spin-independent tunneling are reduced to $t_{\perp}^{\text{TaS}_2, \text{ABA}} = 5.0$ meV and $t_{\perp}^{\text{TaS}_2, \text{AAA}} = 4.5$ meV.

APPENDIX D: DETAILS OF ANALYTICAL PERTURBATIVE CALCULATIONS

We will work with the atomic units by default throughout the derivation here. For example, $\hbar = \mu_B = 1$.

1. Perturbative theory for $\sqrt{(v_{\text{Ising}} k_F \theta)^2 + 4t_{\perp}^2} \gg \Delta$: $C = 12$ topological phases

In this section, we will give a perturbative analysis of the twisted bilayer Hamiltonian given in the main text. We will focus on the regime when $\sqrt{(v_{\text{Ising}} k_F \theta)^2 + 4t_{\perp}^2} \gg \Delta$ and give an explanation of the origin of $C = \pm 12$ topological phases. Mass gaps for all nodes and the phase boundary will also be derived.

a. Construction of the Hamiltonian

Let us start with constructing the effective Hamiltonian. We will consider a small twisting angle θ and keep the $\mathbf{k} \cdot \mathbf{p}$ expansion up to $O(\theta^2)$ (the reason will be given in Appendix D 1 b). As is discussed in the main text, in-plane mirror symmetry prohibits the existence of Rashba SOC, so the monolayer effective Hamiltonian around the intersection point P of the Fermi surface and the Γ - M line simply reads

$$h^{\text{mono}}(\mathbf{k}) = (v_F k_x + a k_y^2) + v_{\text{Ising}} k_y \sigma_z, \quad (\text{D1})$$

where a is the coefficient of the $\mathbf{k} \cdot \mathbf{p}$ expansion. We keep a quadratic term $a k_y^2$ here because it turns out that this term contributes to the leading-order deviation from the linear $\mathbf{k} \cdot \mathbf{p}$ expansion. Equation (D1) can be easily extended to higher orders, and we did use the fitting fourth-order $\mathbf{k} \cdot \mathbf{p}$ in our numerical calculations; see Appendix C.

Without loss of generality, we can consider a bilayer system with the top layer rotated by $\theta/2$ and the bottom layer rotated by $-\theta/2$. This is achieved by simple replacement $k_x \mapsto (k_x + k_F) \cos \frac{\theta}{2} \pm k_y \sin \frac{\theta}{2} - k_F$ and $k_y \mapsto \mp (k_x + k_F) \sin \frac{\theta}{2} + k_y \cos \frac{\theta}{2}$ and expansion still up to θ^2 . The resulting

bilayer Hamiltonian *without* tunneling is then

$$\begin{aligned} h^{\text{without}}(\mathbf{k}) &= \left(v_F k_x + a k_y^2 + \frac{a k_F^2}{4} \theta^2 - \frac{v_F k_F}{8} \theta^2 \right) \\ &+ \left(-a k_F k_y \theta + \frac{\theta}{2} v_F k_y \right) v_z + v_{\text{Ising}} k_y \sigma_z \\ &- v_{\text{Ising}} k_F \frac{\theta}{2} \sigma_z v_z \\ &= \left(v_F k_x + a k_y^2 - \frac{v_2 k_F}{8} \theta^2 \right) + \frac{\theta}{2} v_2 k_y v_z \\ &+ v_{\text{Ising}} k_y \sigma_z - \frac{\theta}{2} v_{\text{Ising}} k_F \sigma_z v_z, \end{aligned} \quad (\text{D2})$$

where v_i are Pauli matrices within the layer space and we defined

$$v_2 \equiv v_F - 2a k_F. \quad (\text{D3})$$

In Eq. (D2), the crucial role played by v_2 is from the second term, which gives the leading-order correction to the wave functions compared with the linear $\mathbf{k} \cdot \mathbf{p}$ expansion. Next, let us try to add interlayer tunnelings to (D2). Based on *two-center approximation* [19], it can be shown that the interlayer tunneling has a weak spatial dependence (see Appendix E) and will be considered as a constant here, $t = t_{\perp}$ (the spin-dependent tunnelings $t_{s,\perp}$ will be included later). We thus have

$$\begin{aligned} h^{\text{bilayer}} &= \left(v_F k_x + a k_y^2 - \frac{v_2 k_F^2}{8} \theta^2 \right) + \frac{\theta}{2} v_2 k_y v_z + v_{\text{Ising}} k_y \sigma_z \\ &- \frac{\theta}{2} v_{\text{Ising}} k_F \sigma_z v_z + t v_x. \end{aligned} \quad (\text{D4})$$

Hamiltonian (D4) reduces to a simple two-band model (and so can be readily diagonalized) for $\sigma_z = \pm 1$. Keeping up to $O(\theta^2)$, we have, for $\sigma_z = +1$,

$$\begin{aligned} \varepsilon_{\pm}^{\uparrow} &= \left(v_F k_x + a k_y^2 - \frac{\theta^2}{8} v_2 k_F \right) + v_{\text{Ising}} k_y \\ &\pm \frac{\Gamma}{2} \left[1 - \frac{v_2 \cdot \cos^2 \xi}{v_{\text{Ising}} k_F} k_y \right] \end{aligned}$$

and, for $\sigma_z = -1$,

$$\begin{aligned} \varepsilon_{\pm}^{\downarrow} &= \left(v_F k_x + a k_y^2 - \frac{\theta^2}{8} v_2 k_F \right) - v_{\text{Ising}} k_y \\ &\pm \frac{\Gamma}{2} \left[1 + \frac{v_2 \cdot \cos^2 \xi}{v_{\text{Ising}} k_F} k_y \right], \end{aligned}$$

where

$$\xi \equiv \arctan \frac{2t}{v_{\text{Ising}} k_F \theta} \quad \text{and} \quad \Gamma \equiv \sqrt{(v_{\text{Ising}} k_F \theta)^2 + 4t^2}.$$

There are some crossing points between the spin-up and spin-down Fermi surfaces. Solving $\varepsilon_{\pm}^{\uparrow} = \varepsilon_{\pm}^{\downarrow} = 0$, we find two such points F and G along the k_x direction (Γ - M line)

$$F = \left(-\frac{\Gamma}{2v_F} + \frac{v_2 k_F \theta^2}{8v_F}, 0 \right), \quad G = \left(+\frac{\Gamma}{2v_F} + \frac{v_2 k_F \theta^2}{8v_F}, 0 \right). \quad (\text{D5})$$

At F , the two low-energy bands come from $\varepsilon_{\pm}^{\uparrow,\downarrow}$, while at G , the two low-energy bands are formed by $\varepsilon_{\pm}^{\uparrow,\downarrow}$. Interestingly,

there are another two such points C and D emergent along the k_y direction that have different low-energy band information:

$$C = \left(-\frac{k_F \theta^2}{8} - \frac{a t^2}{v_F v_{\text{Ising}}^2}, -\frac{\Gamma}{2v_{\text{Ising}}} \right), \quad (\text{D6})$$

$$D = \left(-\frac{k_F \theta^2}{8} - \frac{a t^2}{v_F v_{\text{Ising}}^2}, +\frac{\Gamma}{2v_{\text{Ising}}} \right). \quad (\text{D7})$$

At C , the two low-energy bands are formed by $\varepsilon_{-}^{\uparrow}, \varepsilon_{+}^{\downarrow}$, while at D , the two low-energy bands are formed by $\varepsilon_{+}^{\uparrow}, \varepsilon_{-}^{\downarrow}$. They are all illustrated in Fig. 6.

The low-energy effective Hamiltonian of each node is then the projection of (D4) onto these bands. First of all, we need to read out the eigenstates in v space. Introducing the elevation angle

$$\begin{aligned} \xi_{\pm} &= \arctan \frac{t}{\frac{\theta}{2}(v_2 k_y - v_{\text{Ising}} k_F)} \\ &\simeq \arctan \left[\left(1 \pm \frac{v_2 k_y}{v_{\text{Ising}} k_F} \right) \frac{2t}{v_{\text{Ising}} k_F \theta} \right], \end{aligned}$$

we obtain

$$\begin{aligned} \sigma_z = +1: \quad |v_1\rangle &= \sin \frac{\xi_{+}}{2} |v_{\uparrow}\rangle + \cos \frac{\xi_{+}}{2} |v_{\downarrow}\rangle, \\ |v_2\rangle &= \cos \frac{\xi_{+}}{2} |v_{\uparrow}\rangle - \sin \frac{\xi_{+}}{2} |v_{\downarrow}\rangle, \\ \sigma_z = -1: \quad |v_3\rangle &= \cos \frac{\xi_{-}}{2} |v_{\uparrow}\rangle + \sin \frac{\xi_{-}}{2} |v_{\downarrow}\rangle, \\ |v_4\rangle &= -\sin \frac{\xi_{-}}{2} |v_{\uparrow}\rangle + \cos \frac{\xi_{-}}{2} |v_{\downarrow}\rangle. \end{aligned}$$

We can then lift (D4) into the Nambu representation

$$\begin{aligned} H^{\text{bilayer}} &= \left(v_F k_x + a k_y^2 - \frac{v_2 k_F}{8} \theta^2 \right) \tau_z + \frac{\theta}{2} v_2 k_y v_z \tau_z \\ &+ v_{\text{Ising}} k_y \sigma_z - \frac{\theta}{2} v_{\text{Ising}} k_F \sigma_z v_z + t v_x \tau_x \end{aligned} \quad (\text{D8})$$

and perform the projection. Here, v_i are Pauli matrices for the Nambu space.

We choose the basis as follows.

$$\begin{aligned} \text{At } G: &\{ |\tau_{\uparrow}, \sigma_{\uparrow}, v_2\rangle, |\tau_{\uparrow}, \sigma_{\downarrow}, v_4\rangle, |\tau_{\downarrow}, \sigma_{\uparrow}, v_4\rangle, |\tau_{\downarrow}, \sigma_{\downarrow}, v_2\rangle, \\ &|\tau_{\uparrow}, \sigma_{\uparrow}, v_1\rangle, |\tau_{\uparrow}, \sigma_{\downarrow}, v_3\rangle, |\tau_{\downarrow}, \sigma_{\uparrow}, v_3\rangle, |\tau_{\downarrow}, \sigma_{\downarrow}, v_1\rangle \}, \\ \text{At } F: &\{ |\tau_{\uparrow}, \sigma_{\uparrow}, v_1\rangle, |\tau_{\uparrow}, \sigma_{\downarrow}, v_3\rangle, |\tau_{\downarrow}, \sigma_{\uparrow}, v_3\rangle, |\tau_{\downarrow}, \sigma_{\downarrow}, v_1\rangle, \\ &|\tau_{\uparrow}, \sigma_{\uparrow}, v_2\rangle, |\tau_{\uparrow}, \sigma_{\downarrow}, v_4\rangle, |\tau_{\downarrow}, \sigma_{\uparrow}, v_4\rangle, |\tau_{\downarrow}, \sigma_{\downarrow}, v_2\rangle \}, \\ \text{At } D: &\{ |\tau_{\uparrow}, \sigma_{\uparrow}, v_2\rangle, |\tau_{\uparrow}, \sigma_{\downarrow}, v_3\rangle, |\tau_{\downarrow}, \sigma_{\uparrow}, v_3\rangle, |\tau_{\downarrow}, \sigma_{\downarrow}, v_2\rangle, \\ &|\tau_{\uparrow}, \sigma_{\uparrow}, v_1\rangle, |\tau_{\uparrow}, \sigma_{\downarrow}, v_4\rangle, |\tau_{\downarrow}, \sigma_{\uparrow}, v_4\rangle, |\tau_{\downarrow}, \sigma_{\downarrow}, v_1\rangle \}, \\ \text{At } C: &\{ |\tau_{\uparrow}, \sigma_{\uparrow}, v_1\rangle, |\tau_{\uparrow}, \sigma_{\downarrow}, v_4\rangle, |\tau_{\downarrow}, \sigma_{\uparrow}, v_4\rangle, |\tau_{\downarrow}, \sigma_{\downarrow}, v_1\rangle, \\ &|\tau_{\uparrow}, \sigma_{\uparrow}, v_2\rangle, |\tau_{\uparrow}, \sigma_{\downarrow}, v_3\rangle, |\tau_{\downarrow}, \sigma_{\uparrow}, v_3\rangle, |\tau_{\downarrow}, \sigma_{\downarrow}, v_2\rangle \}. \end{aligned}$$

Then (D8) near F and G can be shown to have the form (for now on, we will also use the coordinate in the momentum space to represent these intersection points: F as \mathbf{F}_{+} , G as \mathbf{F}_{-} , C as \mathbf{C}_{-} , and D as \mathbf{C}_{+})

$$H_0(\mathbf{F}_{\pm}) = v_F \delta k_x \tau_z + v_{\text{Ising}} \delta k_y \sigma_z \pm \Gamma \frac{1 - v_z}{2} \tau_z. \quad (\text{D9})$$

Similarly, near C_{\pm} we have

$$H_0(C_{\pm}) = v_F \delta k_x \tau_z + v_{\text{Ising}} \delta k_y \sigma_z \pm \Gamma \frac{1 - v_z}{2} \sigma_z. \quad (\text{D10})$$

Here, we slightly abuse the notation: Instead of introducing a new symbol, we use the v Pauli matrices to represent the low-energy ($v_z = 1$) and high-energy ($v_z = -1$) subspaces.

b. Low-energy effective theory in Nambu space

The next step is to turn on an in-plane Zeeman exchange field and the intralayer superconducting order parameters Δ . Without loss of generality, below we consider the in-plane Zeeman field to be along the k_y direction, $\mathbf{b} = (0, b_y)$, together with a *spin-dependent hopping* $t_{s,\perp} = t_y$ due to a ferromagnetic layer:

$$H' = b_y \sigma_y + \Delta \cos \frac{\varphi}{2} \cdot \sigma_y \tau_y + \Delta \sin \frac{\varphi}{2} \cdot \sigma_y \tau_x v_z + t_y \sigma_y v_x. \quad (\text{D11})$$

Here, Δ is real, and we add a Josephson phase difference φ between the top and bottom layers through turning on the supercurrent.

Still taking the basis we chose for the low-energy space for each node in the previous section, we have

$$\begin{aligned} H'(F_+) &= -b_y \sin \xi \cdot \sigma_y v_z + \Delta \cos \frac{\varphi}{2} \cdot \sigma_y \tau_y \\ &+ \Delta \cos \xi \sin \frac{\varphi}{2} \cdot \sigma_x \tau_y v_z + b_y \cos \xi \cdot \sigma_y v_x \\ &+ \Delta \sin \xi \sin \frac{\varphi}{2} \cdot \sigma_x \tau_y v_x + t_y \sigma_y, \end{aligned} \quad (\text{D12})$$

$$H'(F_+) = b_y \sin \xi \cdot \sigma_y v_z + \Delta \cos \frac{\varphi}{2} \cdot \sigma_y \tau_y$$

$$\begin{aligned} & - \Delta \cos \xi \sin \frac{\varphi}{2} \cdot \sigma_x \tau_y v_z + b_y \cos \xi \cdot \sigma_y v_x \\ & + \Delta \sin \xi \sin \frac{\varphi}{2} \cdot \sigma_x \tau_y v_x + t_y \sigma_y. \end{aligned} \quad (\text{D13})$$

For C_{\pm} ,

$$\begin{aligned} H'(C_+) &= b_y \cos \xi \cdot \sigma_y + \Delta \cos \frac{\varphi}{2} \cdot \sigma_y \tau_y + \Delta \cos \xi \sin \frac{\varphi}{2} \\ & \cdot \sigma_y \tau_x v_z - b_y \sin \xi \cdot \sigma_x \tau_z v_y + \Delta \sin \xi \sin \frac{\varphi}{2} \cdot \sigma_x \tau_y v_x \\ & - \frac{\Delta}{2v_{\text{Ising}}} \sin^2 \xi \sin \frac{\varphi}{2} \cdot v_2 \theta \cdot \sigma_x \tau_y v_z \\ & + \frac{\Delta}{2v_{\text{Ising}}} \cos \xi \sin \xi \sin \frac{\varphi}{2} \cdot v_2 \theta \cdot \sigma_y \tau_x v_x \\ & - \frac{t_y}{2v_{\text{Ising}}} \sin \xi \cdot v_2 \theta \cdot \sigma_y v_z + t_y \sigma_y v_x, \end{aligned} \quad (\text{D14})$$

$$\begin{aligned} H'(C_-) &= b_y \cos \xi \cdot \sigma_y + \Delta \cos \frac{\varphi}{2} \cdot \sigma_y \tau_y - \Delta \cos \xi \sin \frac{\varphi}{2} \\ & \cdot \sigma_y \tau_x v_z + b_y \sin \xi \cdot \sigma_x \tau_z v_y + \Delta \sin \xi \sin \frac{\varphi}{2} \cdot \sigma_x \tau_y v_x \\ & - \frac{\Delta}{2v_{\text{Ising}}} \sin^2 \xi \sin \frac{\varphi}{2} \cdot v_2 \theta \cdot \sigma_x \tau_y v_z \\ & - \frac{\Delta}{2v_{\text{Ising}}} \cos \xi \sin \xi \sin \frac{\varphi}{2} \cdot v_2 \theta \cdot \sigma_y \tau_x v_x \\ & - \frac{t_y}{2v_{\text{Ising}}} \sin \xi \cdot v_2 \theta \cdot \sigma_y v_z + t_y \sigma_y v_x. \end{aligned} \quad (\text{D15})$$

The effective Hamiltonian for the low-energy sector $|\nu_{\uparrow}\rangle$ then can be obtained from standard perturbation theory. We will keep the θ linear order and the Δ second order. Since both θ and Δ are small, we will drop terms proportional to $\Delta^2 \theta$. Finally,

$$\begin{aligned} H_{\text{eff}}(F_{\pm}) &= v_F \delta k_x \tau_z + v_{\text{Ising}} \delta k_y \sigma_z \mp (b_y \sin \xi \mp t_y) \cdot \sigma_y + \Delta \cos \frac{\varphi}{2} \cdot \sigma_y \tau_y \pm \Delta \cos \xi \sin \frac{\varphi}{2} \cdot \sigma_x \tau_y \\ & \pm \frac{1}{\Gamma} \left[\left[-b_y^2 \cos^2 \xi + \Delta^2 \sin^2 \frac{\varphi}{2} \sin^2 \xi \right] \tau_z + b_y \Delta \sin \frac{\varphi}{2} \sin 2\xi \sigma_z \tau_x \right], \end{aligned} \quad (\text{D16})$$

$$\begin{aligned} H_{\text{eff}}(C_{\pm}) &= v_F \delta k_x \tau_z + v_{\text{Ising}} \delta k_y \sigma_z + b_y \cos \xi \cdot \sigma_y + \Delta \cos \frac{\varphi}{2} \cdot \sigma_y \tau_y \pm \Delta \cos \xi \sin \frac{\varphi}{2} \cdot \sigma_x \tau_x \\ & - \frac{\Delta v_2 \theta}{2v_{\text{Ising}}} \sin^2 \xi \sin \frac{\varphi}{2} \sigma_x \tau_y - \frac{t_y \cdot v_2 \theta}{2v_{\text{Ising}}} \sin \xi \cdot \sigma_y \\ & \pm \frac{1}{\Gamma} \left[\left[b_y^2 + \Delta^2 \sin^2 \xi \right] \sin^2 \xi \cdot \sigma_z \pm 2b_y \Delta \sin^2 \xi \sin \frac{\varphi}{2} \cdot \sigma_z \tau_x + t_y^2 \sigma_z \mp 2b_y t_y \sin \xi \cdot \tau_z \right]. \end{aligned} \quad (\text{D17})$$

c. Topological nodes C and D

Let us first focus on the nodes C and D , i.e., $\mathbf{k} \sim C_{\pm}$. It is convenient to perform a charge rotation $e^{\pm i\zeta/2\tau_z}$ to eliminate the $\pm \Delta \cos \xi \sin \frac{\varphi}{2} \cdot \sigma_y \tau_x$ term in (D17) with $\zeta \equiv \arctan(\cos \xi \tan \frac{\varphi}{2})$. In addition, the σ_y term (and τ_z term) can be absorbed by redefining δk_y (and δk_x). Using $e^{-i\zeta/2\tau_z} \tau_y e^{i\zeta/2\tau_z} = \cos \zeta \cdot \tau_y - \sin \zeta \cdot \tau_x$, we will arrive at

$$\begin{aligned} \tilde{H}_{\text{eff}}(C_{\pm}) &= v_F \delta k_x \tau_z + v_{\text{Ising}} \delta k_y \sigma_z + \left[b_y^{\text{origin}} \cos \xi - \frac{t_y \cdot v_2 \theta}{2v_{\text{Ising}}} \sin \xi \right] \cdot \sigma_y + \tilde{\Delta} \cdot \sigma_y \tau_y \\ & - \frac{\Delta v_2 \theta}{2v_{\text{Ising}}} \sin^2 \xi \sin \frac{\varphi}{2} \cdot \sigma_x \cdot (\cos \zeta \tau_y \mp \sin \zeta \tau_x) + \frac{2b_y \Delta}{\Gamma} \sin^2 \xi \sin \frac{\varphi}{2} \cdot \sigma_z (\cos \zeta \cdot \tau_x \pm \sin \zeta \cdot \tau_y) \\ & = v_F \delta k_x \tau_z + v_{\text{Ising}} \delta k_y \sigma_z + b_y \cos \xi \cdot \sigma_y + \tilde{\Delta} \cdot \sigma_y \tau_y \end{aligned}$$

$$-\frac{\Delta v_2 \theta}{2v_{\text{Ising}}} \sin^2 \xi \sin \frac{\varphi}{2} \cdot \sigma_x \cdot (\cos \zeta \tau_y \mp \sin \zeta \tau_x) + \frac{2b_y \Delta}{\Gamma} \sin^2 \xi \sin \frac{\varphi}{2} \cdot \sigma_z (\cos \zeta \cdot \tau_x \pm \sin \zeta \cdot \tau_y), \quad (\text{D18})$$

with $\tilde{\Delta} = \Delta \sqrt{\cos^2 \frac{\varphi}{2} + \sin^2 \frac{\varphi}{2} \cos^2 \xi} \equiv \Delta \frac{\cos \frac{\varphi}{2}}{\cos \zeta}$. In (D18) we have denoted the original Zeeman fields b_y as b_y^{origin} and rewritten the σ_y term as $b_y \cos \xi$ by introducing a new shifted field

$$b_y \equiv b_y^{\text{origin}} - \frac{t_y \cdot v_2 \theta}{2v_{\text{Ising}}} \tan \xi = b_y^{\text{origin}} - \frac{t_y \cdot v_2 t}{v_{\text{Ising}}^2 k_F}.$$

This is actually why we introduce the spin-dependent tunneling together with the the Zeeman fields.

Starting with the linear-order effective Hamiltonian [the first line of (D18), so \mathbf{C}_{\pm} has the same form], we find that a pair of Dirac nodes $\mathbf{k}_0^{\pm} \equiv (\pm k_{x,0}^{\pm}, 0)$ along the δk_x direction emerges when $b_y \cos \xi > \tilde{\Delta}$. Repeating the two-band effective theory analysis (separating for $\sigma_y = \pm 1$), we find, near the \mathbf{k}_0^{\pm} Dirac nodes,

$$h_{\text{eff}\pm}^{\pm}(\mathbf{C}) = \pm(-v_F \cos \theta^+ \cdot \delta k_x \mu_z + v_{\text{Ising}} \sin \theta^+ \cdot \delta k_y \mu_x), \quad (\text{D19})$$

where

$$\theta^+ = \arctan \frac{\tilde{\Delta}}{v_F k_{x,0}^+}, \quad k_{x,0}^+ = \frac{1}{v_F} \sqrt{(b_y \cos \xi)^2 - \tilde{\Delta}^2}.$$

These effective theories are obtained in the basis

$$\begin{aligned} |\psi_1^+\rangle &= |\sigma_y = 1\rangle \otimes \left(i \sin \frac{\theta^+}{2} |\tau_z, \uparrow\rangle + \cos \frac{\theta^+}{2} |\tau_z, \downarrow\rangle \right), \\ |\psi_2^+\rangle &= |\sigma_y = -1\rangle \otimes \left(\cos \frac{\theta^+}{2} |\tau_z, \uparrow\rangle - i \sin \frac{\theta^+}{2} |\tau_z, \downarrow\rangle \right), \\ |\psi_1^-\rangle &= |\sigma_y = 1\rangle \otimes \left(\cos \frac{\theta^+}{2} |\tau_z, \uparrow\rangle - i \sin \frac{\theta^+}{2} |\tau_z, \downarrow\rangle \right), \\ |\psi_2^-\rangle &= |\sigma_y = -1\rangle \otimes \left(i \sin \frac{\theta^+}{2} |\tau_z, \uparrow\rangle + \cos \frac{\theta^+}{2} |\tau_z, \downarrow\rangle \right). \end{aligned}$$

To be concrete, states $|\sigma_y = \pm 1\rangle$ are defined as $|\sigma_y = 1\rangle = \frac{1}{\sqrt{2}}(|\sigma_z, \uparrow\rangle + i|\sigma_z, \downarrow\rangle)$ and $|\sigma_y = -1\rangle = \frac{1}{\sqrt{2}}(i|\sigma_z, \uparrow\rangle + |\sigma_z, \downarrow\rangle)$.

The remaining task is to project the last line of (D18) (as the perturbation) onto this low-energy basis. We get, for \mathbf{C}_+ ,

$$\begin{aligned} \text{At } \mathbf{k}_0^+ : \frac{\Delta v_2 \theta}{2v_{\text{Ising}}} \sin^2 \xi \sin \frac{\varphi}{2} (\sin \zeta \cos \theta^+ \mu_x + \cos \zeta \mu_y) \\ + \frac{2b_y \Delta}{\Gamma} \sin^2 \xi \sin \frac{\varphi}{2} \cdot (-\cos \zeta \cos \theta^+ \mu_y - \sin \zeta \mu_x), \end{aligned} \quad (\text{D20})$$

$$\begin{aligned} \text{At } \mathbf{k}_0^- : \frac{\Delta v_2 \theta}{2v_{\text{Ising}}} \sin^2 \xi \sin \frac{\varphi}{2} (\sin \zeta \cos \theta^+ \mu_x - \cos \zeta \mu_y) \\ + \frac{2b_y \Delta}{\Gamma} \sin^2 \xi \sin \frac{\varphi}{2} \cdot (-\cos \zeta \cos \theta^+ \mu_y + \sin \zeta \mu_x) \end{aligned} \quad (\text{D21})$$

and, for \mathbf{C}_- ,

$$\text{At } \mathbf{k}_0^+ : \frac{\Delta v_2 \theta}{2v_{\text{Ising}}} \sin^2 \xi \sin \frac{\varphi}{2} (-\sin \zeta \cos \theta^+ \mu_x + \cos \zeta \mu_y)$$

$$+ \frac{2b_y \Delta}{\Gamma} \sin^2 \xi \sin \frac{\varphi}{2} \cdot (-\cos \zeta \cos \theta^+ \mu_y + \sin \zeta \mu_x), \quad (\text{D22})$$

$$\begin{aligned} \text{At } \mathbf{k}_0^- : \frac{\Delta v_2 \theta}{2v_{\text{Ising}}} \sin^2 \xi \sin \frac{\varphi}{2} (-\sin \zeta \cos \theta^+ \mu_x - \cos \zeta \mu_y) \\ + \frac{2b_y \Delta}{\Gamma} \sin^2 \xi \sin \frac{\varphi}{2} \cdot (-\cos \zeta \cos \theta^+ \mu_y - \sin \zeta \mu_x). \end{aligned} \quad (\text{D23})$$

The new μ_x terms brought by the perturbation just shift the nodes, while the new μ_y terms brought by the perturbation open gaps. Collecting all μ_y terms, we get the four masses m_{\pm} (each value is twofold degenerate) for the nodes split from intersection points C and D :

$$\begin{aligned} m_{\pm}(\mathbf{C}_{\pm}) &= \frac{2b_y \Delta}{\Gamma} \sin^2 \xi \sin \frac{\varphi}{2} \cos \zeta \cos \theta^+ \\ &\times \left(1 \pm \frac{c\theta\Gamma}{4b_y v_{\text{Ising}} \cos \theta^+} \right) \equiv m(1 \pm \delta). \end{aligned} \quad (\text{D24})$$

Clearly, it is the dimensionless number $\delta \equiv \frac{c\theta\Gamma}{4b_y v_{\text{Ising}} \cos \theta^+}$ that dominates the topology around \mathbf{C}_{\pm} . If $|\delta| < 1$, we find that all four Dirac nodes generate masses of *the same sign*, resulting in a total transfer of Chern number ± 4 for one intersection point P . Therefore the whole heterostructure gains a Chern number 12 with the C_{3z} -rotation symmetry.

In terms of the original parameters, such a condition reduces to

$$v_2 t^2 < \Delta k_F v_{\text{Ising}}^2 a(\xi, \varphi) \sqrt{\left(\frac{b_y}{b_c^{\text{topo}}} \right)^2 - 1}, \quad (\text{D25})$$

with

$$b_c^{\text{topo}} \equiv \Delta \sqrt{\sec^2 \xi \cos^2 \frac{\varphi}{2} + \sin^2 \frac{\varphi}{2}} \quad (\text{D26})$$

and

$$a(\xi, \varphi) = \tan \xi \sin \xi \sqrt{\sec^2 \xi \cos^2 \frac{\varphi}{2} + \sin^2 \frac{\varphi}{2}}.$$

As for the mass gap, in terms of original parameters, we have

$$\begin{aligned} m &\equiv \frac{2b_y \Delta}{\Gamma} \sin^2 \xi \sin \frac{\varphi}{2} \cos \zeta \cos \theta^+ \\ &= \sin 2 \frac{\varphi}{2} \frac{\Delta^2 \sin^2 \xi}{v_{\text{Ising}} k_F \theta} \sqrt{\frac{(b_y/\Delta)^2}{\sec^2 \xi \cos^2 \frac{\varphi}{2} + \sin^2 \frac{\varphi}{2}} - 1} \\ &\equiv \sin \varphi \frac{\Delta^2 \sin^2 \xi}{v_{\text{Ising}} k_F \theta} \sqrt{\left(\frac{b_y}{b_c^{\text{topo}}} \right)^2 - 1}. \end{aligned} \quad (\text{D27})$$

Recall that φ is the Josephson phase difference, which we do not require to be small; therefore $\xi = \arctan \frac{2t}{v_{\text{Ising}} k_F \theta}$. To have a meaningful topological gap, fraction b_y/Δ must be large enough that the quantity inside the square root is positive definite. This requirement is satisfied for the two candidates,

NbSe₂ and TaS₂, that we proposed in the main text—which support large in-plane magnetic fields that are far beyond the Pauli limit.

d. Trivial nodes F and G

Finally, let us look at the intersection points F and G , i.e., $\mathbf{k} \sim \mathbf{F}_\pm$. Still we can absorb the last term of (D16) by redefining δk_x . After that we get

$$\begin{aligned} \tilde{H}_{\text{eff}}(\mathbf{F}_\pm) &= v_F \delta \tilde{k}_x \tau_z + v_{\text{Ising}} \delta k_y \sigma_z \mp (b_y^{\text{origin}} \sin \xi \mp t_y) \cdot \sigma_y \\ &+ \Delta \cos \frac{\varphi}{2} \cdot \sigma_y \tau_y \pm \Delta \cos \xi \sin \frac{\varphi}{2} \cdot \sigma_x \tau_y \\ &\pm \frac{1}{\Gamma} b_y^{\text{origin}} \Delta \sin \frac{\varphi}{2} \sin 2\xi \sigma_z \tau_x. \end{aligned} \quad (\text{D28})$$

Without bothering to perform the projection one more time, as we have done for C_\pm , it is helpful to notice an effective ($\delta k_x \mapsto -\delta k_x$) mirror symmetry τ_y for the Δ -linear-order effective Hamiltonian $\tilde{H}_{\text{eff}}(\mathbf{F}_\pm)$. Therefore the *total Chern number must vanish* for the effective theory of each intersection point (F and G). The gap position can be easily solved from the first line of (D28):

$$\tilde{k}_x = \pm \frac{1}{v_F} \sqrt{(b_y^{\text{origin}} \sin \xi - t_y)^2 - \Delta^2 \cos^2 \frac{\varphi}{2}},$$

with the gap size

$$m(\mathbf{F}_\pm) = \Delta \cos \xi \sin \frac{\varphi}{2}. \quad (\text{D29})$$

As a side remark, if one includes the second-order perturbation, it can be shown that the second-order gap is always much smaller than the linear-order gap (D29) in the current perturbative regime.

2. A different perturbative regime: $C = 6$ topological phases

In this section we briefly discuss the Chern number $C = 6$ topological phases in a different perturbative regime. We start with the limit that the spin-independent hopping and the twisting angle both vanish: $t_\perp = 0$, $\theta = 0$. In addition, we fix the spin-dependent hopping to be the same as the Zeeman exchange field $t_y = b_y$ as is set in case (i) in the main text.

The full linear-order $\mathbf{k} \cdot \mathbf{p}$ BCS Hamiltonian near point P reads

$$\begin{aligned} H_{\text{BCS}}^{\text{bilayer}}(\mathbf{k}) &= v_F k_x \tau_z + v_{\text{Ising}} k_y \sigma_z + \cos \frac{\varphi}{2} \Delta \sigma_y \tau_y \\ &+ \sin \frac{\varphi}{2} \Delta \sigma_y \tau_x v_z - v_{\text{Ising}} k_F \theta / 2 \sigma_z v_z + b_y \sigma_y \\ &+ t_y \sigma_y v_x + t \tau_z v_x. \end{aligned} \quad (\text{D30})$$

More precisely, our strategy is to first consider the situation of $t_y = b_y \sim \Delta$ with $t_\perp = 0$, $\theta = 0$, and then turn on a small $t_\perp \ll \Delta$ and a small twisting angle $v_{\text{Ising}} k_F \theta \ll \Delta$ as perturbations. This exactly corresponds to the perturbative regime in the numerical phase diagrams where $C = 6$ is realized.

One way to see the origin of the $C = 6$ phase is to realize that when $t_y = b_y$, only the $v_x = 1$ subspace (a half of the

bands) experiences the magnetism captured by the two terms $b_y \sigma_y + t_y \sigma_y v_x$. Therefore, even without detailed node analyses as is done in the $C = 12$ regime, we know that, instead of four topological Dirac nodes, in the present situation the Hamiltonian (D30) only gives *two* topological Dirac nodes when $t_y = b_y$ is tuned up. After a small $t_\perp \ll \Delta$ and a small twisting angle $v_{\text{Ising}} k_F \theta \ll \Delta$ are turned on, these nodes receive a topological mass gap, and the $C = 6$ phase is realized (due to the C_{3z} -rotation symmetry).

APPENDIX E: TWO-CENTER APPROXIMATION

Given two Bloch states $|\psi_{\mathbf{k},\alpha}^u\rangle$ and $|\psi_{\mathbf{k}',\beta}^d\rangle$ from the top and bottom layer with the crystal momentum \mathbf{k} and \mathbf{k}' and sublattice labels α and β , the two-center approximation [19] tells us that the tunneling strength between these two states takes the general form [63,64]

$$\begin{aligned} t_{\mathbf{k},\mathbf{k}'}^{\alpha\beta} &\equiv \langle \psi_{\mathbf{k},\alpha}^u | H | \psi_{\mathbf{k}',\beta}^d \rangle = \frac{1}{V} \sum_{\mathbf{G}_1, \mathbf{G}_2} \delta_{\mathbf{k}+\mathbf{G}_1, \mathbf{k}'+\mathbf{G}_2} \\ &\cdot e^{-i\mathbf{G}_2 \cdot \boldsymbol{\tau}_{2\beta}} \cdot t^{\alpha\beta}(\mathbf{k} + \mathbf{G}_1) \cdot e^{i\mathbf{G}_1 \cdot \boldsymbol{\tau}_{1\alpha}} \end{aligned} \quad (\text{E1})$$

if one expands the Bloch state with the Wannier basis for each layer, i.e., $t^{\alpha\beta}(\mathbf{k} - \mathbf{G}_2) \equiv \langle \mathbf{R}_1 + \boldsymbol{\tau}_1 | H | \mathbf{R}_2 + \boldsymbol{\tau}_2 \rangle$ with $\boldsymbol{\tau}_{1,2}$ being the sublattice vectors, and makes use of the Poisson resummation formula [65]. Here, \mathbf{G}_1 and \mathbf{G}_2 are reciprocal vectors of the top and bottom layer, respectively.

The allowed tunneling processes are constrained by the delta function in (E1), while its concrete form mainly comes from the two exponentials. More concretely, let us consider the bilayer system with the top layer rotated by a small angle $\theta/2$, and the bottom layer rotated by $-\theta/2$, and focus on the region around the intersection point P : $\mathbf{k} = \mathbf{k}_p^t + \mathbf{F}^t$ and $\mathbf{k}' = \mathbf{k}_p^b + \mathbf{F}^b$ with $|\mathbf{F}^{t,b}| \ll 1$. Since the real-space tunneling $t(\mathbf{r}^t - \mathbf{r}^b)$ is a function of the spatial separation of two Wannier states $\sqrt{(\mathbf{r}^t - \mathbf{r}^b)^2 + |\mathbf{d}_\perp|^2}$, where interlayer spacing $|\mathbf{d}_\perp| \gg O(|\mathbf{r}^t - \mathbf{r}^b|)$, it should be flat enough in a large region of real space (to the same order as the moiré pattern). Accordingly, $t^{\alpha\beta}(\mathbf{k}_p^t + \mathbf{F}^t + \mathbf{G}_1) \simeq t^{\alpha\beta}(\mathbf{k}_p^t + \mathbf{G}_1)$ is a good approximation, and the summation over the Brillouin zone (BZ) of each layer in (E1) can be easily done.

(a) Since $|\mathbf{F}^{t,b}| \ll 1$, the Kronecker delta function in (E1) is nonvanishing only if \mathbf{G}_1 and \mathbf{G}_2 differ by a small rotation. Namely,

$$t_{\mathbf{F}^t, \mathbf{F}^b}^{\alpha\beta} = \frac{1}{V} \sum_{\mathbf{G}_1, \mathbf{G}_2} \delta_{\mathbf{G}_1, \mathbf{G}_2} \cdot e^{-i\mathbf{G}_2 \cdot \boldsymbol{\tau}_{2\beta}} \cdot t^{\alpha\beta}(\mathbf{k}_p + \mathbf{G}_1) \cdot e^{i\mathbf{G}_1 \cdot \boldsymbol{\tau}_{1\alpha}}.$$

(b) Since the threefold intersection point P is *not* connected with the reciprocal vectors for each layer (as a sharp contrast, in twisted bilayer graphene the threefold K valleys are directly connected with some reciprocal vectors—this is actually how the moiré pattern enters into constraining the form of tunneling terms), the above summation only needs to count the branch with $\mathbf{G}_1 = \mathbf{G}_2 = \mathbf{0}$.

As a result, we find that the tunneling strength only has a trivial momentum dependence $t_{\mathbf{F}^t, \mathbf{F}^b}^{\alpha\beta} = t$.

- [1] C.-S. Lian, C. Si, and W. Duan, *Nano Lett.* **18**, 2924 (2018).
- [2] M. He, P. Rivera, D. Van Tuan, N. P. Wilson, M. Yang, T. Taniguchi, K. Watanabe, J. Yan, D. G. Mandrus, H. Yu, H. Dery, W. Yao, and X. Xu, *Nat. Commun.* **11**, 618 (2020).
- [3] A. M. Jones, H. Yu, N. J. Ghimire, S. Wu, G. Aivazian, J. S. Ross, B. Zhao, J. Yan, D. G. Mandrus, D. Xiao, W. Yao, and X. Xu, *Nat. Nanotechnol.* **8**, 634 (2013).
- [4] P. Rivera, K. L. Seyler, H. Yu, J. R. Schaibley, J. Yan, D. G. Mandrus, W. Yao, and X. Xu, *Science* **351**, 688 (2016).
- [5] W. Li, X. Lu, J. Wu, and A. Srivastava, *Nat. Nanotechnol.* **16**, 148 (2021).
- [6] D. Costanzo, S. Jo, H. Berger, and A. F. Morpurgo, *Nat. Nanotechnol.* **11**, 339 (2016).
- [7] R. Yan, G. Khalsa, B. T. Schaefer, A. Jarjour, S. Rouvimov, K. C. Nowack, H. G. Xing, and D. Jena, *Appl. Phys. Express* **12**, 023008 (2019).
- [8] C.-w. Cho, J. Lyu, C. Y. Ng, J. J. He, K. T. Lo, D. Chareev, T. A. Abdel-Baset, M. Abdel-Hafiez, and R. Lortz, *Nat. Commun.* **12**, 3676 (2021).
- [9] S. C. de la Barrera, M. R. Sinko, D. P. Gopalan, N. Sivadas, K. L. Seyler, K. Watanabe, T. Taniguchi, A. W. Tsun, X. Xu, D. Xiao, and B. M. Hunt, *Nat. Commun.* **9**, 1427 (2018).
- [10] L. Li, X. Deng, Z. Wang, Y. Liu, M. Abeykoon, E. Dooryhee, A. Tomic, Y. Huang, J. B. Warren, E. S. Bozin, S. J. L. Billinge, Y. Sun, Y. Zhu, G. Kotliar, and C. Petrovic, *npj Quantum Mater.* **2**, 11 (2017).
- [11] C.-S. Lian, C. Heil, X. Liu, C. Si, F. Giustino, and W. Duan, *J. Phys. Chem. Lett.* **10**, 4076 (2019).
- [12] X. Cai, T. Song, N. P. Wilson, G. Clark, M. He, X. Zhang, T. Taniguchi, K. Watanabe, W. Yao, D. Xiao, M. A. McGuire, D. H. Cobden, and X. Xu, *Nano Lett.* **19**, 3993 (2019).
- [13] G. Aivazian, Z. Gong, A. M. Jones, R.-L. Chu, J. Yan, D. G. Mandrus, C. Zhang, D. Cobden, W. Yao, and X. Xu, *Nat. Phys.* **11**, 148 (2015).
- [14] M. A. McGuire, G. Clark, S. KC, W. M. Chance, G. E. Jellison Jr, V. R. Cooper, X. Xu, and B. C. Sales, *Phys. Rev. Mater.* **1**, 014001 (2017).
- [15] L. Ai, E. Zhang, J. Yang, X. Xie, Y. Yang, Z. Jia, Y. Zhang, S. Liu, Z. Li, P. Leng, X. Cao, X. Sun, T. Zhang, X. Kou, Z. Han, F. Xiu, and S. Dong, *Nat. Commun.* **12**, 6580 (2021).
- [16] H. Idzuchi, F. Pientka, K.-F. Huang, K. Harada, Ö. Gül, Y. Shin, L. Nguyen, N. Jo, D. Shindo, R. Cava, P. C. Canfield, and P. Kim, *arXiv:2012.14969*.
- [17] Y. Cao, V. Fatemi, A. Demir, S. Fang, S. L. Tomarken, J. Y. Luo, J. D. Sanchez-Yamagishi, K. Watanabe, T. Taniguchi, E. Kaxiras, R. C. Ashoori, and P. Jarillo-Herrero, *Nature (London)* **556**, 80 (2018).
- [18] Y. Cao, V. Fatemi, S. Fang, K. Watanabe, T. Taniguchi, E. Kaxiras, and P. Jarillo-Herrero, *Nature (London)* **556**, 43 (2018).
- [19] R. Bistritzer and A. H. MacDonald, *Proc. Natl. Acad. Sci. USA* **108**, 12233 (2011).
- [20] H. Li, S. Li, M. H. Naik, J. Xie, X. Li, J. Wang, E. Regan, D. Wang, W. Zhao, S. Zhao, S. Kahn, K. Yumigeta, M. Blei, T. Taniguchi, K. Watanabe, S. Tongay, A. Zettl, S. G. Louie, F. Wang, and M. F. Crommie, *Nat. Mater.* **20**, 945 (2021).
- [21] T. Devakul, V. Crépel, Y. Zhang, and L. Fu, *Nat. Commun.* **12**, 6730 (2021).
- [22] M. Angeli and A. H. MacDonald, *Proc. Natl. Acad. Sci. USA* **118**, e2021826118 (2021).
- [23] F. Wu, T. Lovorn, E. Tutuc, I. Martin, and A. H. MacDonald, *Phys. Rev. Lett.* **122**, 086402 (2019).
- [24] O. Can, T. Tummuru, R. P. Day, I. Elfimov, A. Damascelli, and M. Franz, *Nat. Phys.* **17**, 519 (2021).
- [25] X.-Y. Song, Y.-H. Zhang, and A. Vishwanath, *Phys. Rev. B* **105**, L201102 (2022).
- [26] S. Zhao, N. Poccia, X. Cui, P. A. Volkov, H. Yoo, R. Engelke, Y. Ronen, R. Zhong, G. Gu, S. Plugge, T. Tummuru, M. Franz, J. H. Pixley, and P. Kim, *arXiv:2108.13455*.
- [27] P. A. Volkov, J. H. Wilson, and J. Pixley, *arXiv:2012.07860*.
- [28] P. A. Volkov, S. Y. F. Zhao, N. Poccia, X. Cui, P. Kim, and J. Pixley, *arXiv:2108.13456*.
- [29] D. Shaffer, J. Kang, F. J. Burnell, and R. M. Fernandes, *Phys. Rev. B* **101**, 224503 (2020).
- [30] W.-Y. He, B. T. Zhou, J. J. He, N. F. Yuan, T. Zhang, and K. T. Law, *Commun. Phys.* **1**, 40 (2018).
- [31] X. Xi, Z. Wang, W. Zhao, J.-H. Park, K. T. Law, H. Berger, L. Forró, J. Shan, and K. F. Mak, *Nat. Phys.* **12**, 139 (2016).
- [32] Y. Xing, K. Zhao, P. Shan, F. Zheng, Y. Zhang, H. Fu, Y. Liu, M. Tian, C. Xi, H. Liu, J. Feng, X. Lin, S. Ji, X. Chen, Q.-K. Xue, and J. Wang, *Nano Lett.* **17**, 6802 (2017).
- [33] E. Navarro-Moratalla, J. O. Island, S. Manas-Valero, E. Pinilla-Cienfuegos, A. Castellanos-Gomez, J. Quereda, G. Rubio-Bollinger, L. Chirolli, J. A. Silva-Guillén, N. Agrait, G. A. Steele, F. Guinea, H. S. J. van der Zant, and E. Coronado, *Nat. Commun.* **7**, 11043 (2016).
- [34] L. Xian, D. M. Kennes, N. Tancogne-Dejean, M. Altarelli, and A. Rubio, *Nano Lett.* **19**, 4934 (2019).
- [35] X. Lu, R. Fei, L. Zhu, and L. Yang, *Nat. Commun.* **11**, 4724 (2020).
- [36] F. Zhang, H. Zhang, W. Mi, and X. Wang, *Phys. Chem. Chem. Phys.* **22**, 8647 (2020).
- [37] H.-R. Fuh, C.-R. Chang, Y.-K. Wang, R. F. Evans, R. W. Chantrell, and H.-T. Jeng, *Sci. Rep.* **6**, 32625 (2016).
- [38] W. Zhang, L. Zhang, P. K. J. Wong, J. Yuan, G. Vinai, P. Torelli, G. van der Laan, Y. P. Feng, and A. T. Wee, *ACS Nano* **13**, 8997 (2019).
- [39] S. Kezilebieke, M. N. Huda, P. Dreher, I. Manninen, Y. Zhou, J. Sainio, R. Mansell, M. M. Ugeda, S. van Dijken, H.-P. Komsa, and P. Liljeroth, *Commun. Phys.* **3**, 116 (2020).
- [40] F. Aikebaier, T. T. Heikkilä, and J. L. Lado, *Phys. Rev. B* **105**, 054506 (2022).
- [41] D. Zhong, K. L. Seyler, X. Linpeng, R. Cheng, N. Sivadas, B. Huang, E. Schmidgall, T. Taniguchi, K. Watanabe, M. A. McGuire, W. Yao, D. Xiao, K.-M. C. Fu, and X. Xu, *Sci. Adv.* **3**, e1603113 (2017).
- [42] D. Zhong, K. L. Seyler, X. Linpeng, N. P. Wilson, T. Taniguchi, K. Watanabe, M. A. McGuire, K.-M. C. Fu, D. Xiao, W. Yao, and X. Xu, *Nat. Nanotechnol.* **15**, 187 (2020).
- [43] K. L. Seyler, D. Zhong, B. Huang, X. Linpeng, N. P. Wilson, T. Taniguchi, K. Watanabe, W. Yao, D. Xiao, M. A. McGuire, K.-M. C. Fu, and X. Xu, *Nano Lett.* **18**, 3823 (2018).
- [44] K. Zollner, P. E. Faria Junior, and J. Fabian, *Phys. Rev. B* **100**, 085128 (2019).
- [45] L. Ciorciaro, M. Kroner, K. Watanabe, T. Taniguchi, and A. Imamoglu, *Phys. Rev. Lett.* **124**, 197401 (2020).
- [46] J. Pan, C. Guo, C. Song, X. Lai, H. Li, W. Zhao, H. Zhang, G. Mu, K. Bu, T. Lin, X. Xie, M. Chen, and F. Huang, *J. Am. Chem. Soc.* **139**, 4623 (2017).

- [47] G.-B. Liu, W.-Y. Shan, Y. Yao, W. Yao, and D. Xiao, *Phys. Rev. B* **88**, 085433 (2013).
- [48] Γ - M mirror symmetry protects that there is no singlet-triplet mixing at the P point.
- [49] M. M. Ugeda, A. J. Bradley, Y. Zhang, S. Onishi, Y. Chen, W. Ruan, C. Ojeda-Aristizabal, H. Ryu, M. T. Edmonds, H.-Z. Tsai, A. Riss, S.-K. Mo, D. Lee, A. Zettl, Z. Hussain, Z.-X. Shen, and M. F. Crommie, *Nat. Phys.* **12**, 92 (2016).
- [50] X. Xi, L. Zhao, Z. Wang, H. Berger, L. Forró, J. Shan, and K. F. Mak, *Nat. Nanotechnol.* **10**, 765 (2015).
- [51] Y. Nakata, K. Sugawara, S. Ichinokura, Y. Okada, T. Hitosugi, T. Koretsune, K. Ueno, S. Hasegawa, T. Takahashi, and T. Sato, *npj 2D Mater. Appl.* **2**, 12 (2018).
- [52] In Ref. [9], a smaller value of tunneling of about 15 meV for bilayer NbSe₂ is reported. We ascribe such a discrepancy to the choice of van der Waals pseudopotentials.
- [53] Y. Yang, S. Fang, V. Fatemi, J. Ruhman, E. Navarro-Moratalla, K. Watanabe, T. Taniguchi, E. Kaxiras, and P. Jarillo-Herrero, *Phys. Rev. B* **98**, 035203 (2018).
- [54] For few-layer TaS₂, the relation is also reported to be $\Delta_0 = 2.2k_B T_{c0}$ by E. Sohn, X. Xi, W.-Y. He, S. Jiang, Z. Wang, K. Kang, J.-H. Park, H. Berger, L. Forró, K. T. Law, J. Shan, and K. F. Mak [*Nat. Mater.* **17**, 504 (2018)]. Since such a coefficient is material and stacking dependent, we will still take the value of the BCS approximation $\Delta_0 = 1.76k_B T_{c0}$ as a demonstration.
- [55] P. Giannozzi, S. Baroni, N. Bonini, M. Calandra, R. Car, C. Cavazzoni, D. Ceresoli, G. L. Chiarotti, M. Cococcioni, I. Dabo, A. Dal Corso, S. de Gironcoli, S. Fabris, G. Fratesi, R. Gebauer, U. Gerstmann, C. Gougoussis, A. Kokalj, M. Lazzeri, L. Martin-Samos *et al.*, *J. Phys.: Condens. Matter* **21**, 395502 (2009).
- [56] P. Giannozzi, O. Andreussi, T. Brumme, O. Bunau, M. B. Nardelli, M. Calandra, R. Car, C. Cavazzoni, D. Ceresoli, M. Cococcioni, N. Colonna, I. Carnimeo, A. Dal Corso, S. de Gironcoli, P. Delugas, R. A. DiStasio Jr, A. Ferretti, A. Floris, G. Fratesi, G. Fugallo *et al.*, *J. Phys.: Condens. Matter* **29**, 465901 (2017).
- [57] G. Pizzi, V. Vitale, R. Arita, S. Blügel, F. Freimuth, G. Géranton, M. Gibertini, D. Gresch, C. Johnson, T. Koretsune, J. Ibañez-Azpiroz, H. Lee, J.-M. Lihm, D. Marchand, A. Marrazzo, Y. Mokrousov, J. I. Mustafa, Y. Nohara, Y. Nomura, L. Paulatto *et al.*, *J. Phys.: Condens. Matter* **32**, 165902 (2020).
- [58] A. Tkatchenko and M. Scheffler, *Phys. Rev. Lett.* **102**, 073005 (2009).
- [59] K. Berland, D. Chakraborty, and T. Thonhauser, *Phys. Rev. B* **99**, 195418 (2019).
- [60] K. Lee, É. D. Murray, L. Kong, B. I. Lundqvist, and D. C. Langreth, *Phys. Rev. B* **82**, 081101(R) (2010).
- [61] V. R. Cooper, *Phys. Rev. B* **81**, 161104(R) (2010).
- [62] We use the crystalline data from SpringerMaterials; see https://materials.springer.com/isp/crystallographic/docs/sd_0457067 and https://materials.springer.com/isp/crystallographic/docs/sd_0551013.
- [63] G. Catarina, B. Amorim, E. V. Castro, J. M. Lopes, and N. M. Peres, in *Graphene-like 2D Materials*, Handbook of Graphene Vol. 3 (Wiley, New York, 2019), Chap. 6, pp. 177–231.
- [64] R. Bistritzer and A. H. MacDonald, *Phys. Rev. B* **81**, 245412 (2010).
- [65] P. J. Ledwith, G. Tarnopolsky, E. Khalaf, and A. Vishwanath, Fractional Chern insulator states in twisted bilayer graphene: An analytical approach, *Phys. Rev. Res.* **2**, 023237 (2020).